

Library Declaration and Deposit Agreement

1. STUDENT DETAILS

Please complete the following:

Full name:

University ID number:

2. THESIS DEPOSIT

2.1 Under your registration at the University, you are required to deposit your thesis with the University in BOTH hard copy and in digital format. The digital copy should normally be saved as a single pdf file.

2.2 The hard copy will be housed in the University Library. The digital copy will be deposited in the University's Institutional Repository (WRAP). Unless otherwise indicated (see 2.6 below), this will be made immediately openly accessible on the Internet and will be supplied to the British Library to be made available online via its Electronic Theses Online Service (EThOS) service.
[At present, theses submitted for a Master's degree by Research (MA, MSc, LLM, MS or MMedSci) are not being deposited in WRAP and not being made available via EthOS. This may change in future.]

2.3 In exceptional circumstances, the Chair of the Board of Graduate Studies may grant permission for an embargo to be placed on public access to the thesis **in excess of two years**. This must be applied for when submitting the thesis for examination (further information is available in the *Guide to Examinations for Higher Degrees by Research*.)

2.4 If you are depositing a thesis for a Master's degree by Research, the options below only relate to the hard copy thesis.

2.5 If your thesis contains material protected by third party copyright, you should consult with your department, and if appropriate, deposit an abridged hard and/or digital copy thesis.

2.6 Please tick one of the following options for the availability of your thesis (guidance is available in the *Guide to Examinations for Higher Degrees by Research*):

- Both the hard and digital copy thesis can be made publicly available immediately
- The hard copy thesis can be made publicly available immediately and the digital copy thesis can be made publicly available after a period of two years (*should you subsequently wish to reduce the embargo period please inform the Library*)
- Both the hard and digital copy thesis can be made publicly available after a period of two years (*should you subsequently wish to reduce the embargo period please inform the Library*)

- Both the hard copy and digital copy thesis can be made publicly available after _____ (insert time period in excess of two years). **This option requires the prior approval of the Chair of the Board of Graduate Studies (see 2.3 above)**

2.7 The University encourages users of the Library to utilise theses as much as possible, and unless indicated below users will be able to photocopy your thesis.

- I do not wish for my thesis to be photocopied

3. GRANTING OF NON-EXCLUSIVE RIGHTS

Whether I deposit my Work personally or through an assistant or other agent, I agree to the following:
Rights granted to the University of Warwick and the British Library and the user of the thesis through

this agreement are non-exclusive. I retain all rights in the thesis in its present version or future versions. I agree that the institutional repository administrators and the British Library or their agents may, without changing content, digitise and migrate the thesis to any medium or format for the purpose of future preservation and accessibility.

4. DECLARATIONS

I DECLARE THAT:

I am the author and owner of the copyright in the thesis and/or I have the authority of the authors and owners of the copyright in the thesis to make this agreement. Reproduction of any part of this thesis for teaching or in academic or other forms of publication is subject to the normal limitations on the use of copyrighted materials and to the proper and full acknowledgement of its source.

The digital version of the thesis I am supplying is either the same version as the final, hard-bound copy submitted in completion of my degree once any minor corrections have been completed, or is an abridged version (see 2.5 above).

I have exercised reasonable care to ensure that the thesis is original, and does not to the best of my knowledge break any UK law or other Intellectual Property Right, or contain any confidential material.

I understand that, through the medium of the Internet, files will be available to automated agents, and may be searched and copied by, for example, text mining and plagiarism detection software.

At such time that my thesis will be made publically available digitally (see 2.6 above), I grant the University of Warwick and the British Library a licence to make available on the Internet the thesis in digitised format through the Institutional Repository and through the British Library via the EThOS service.

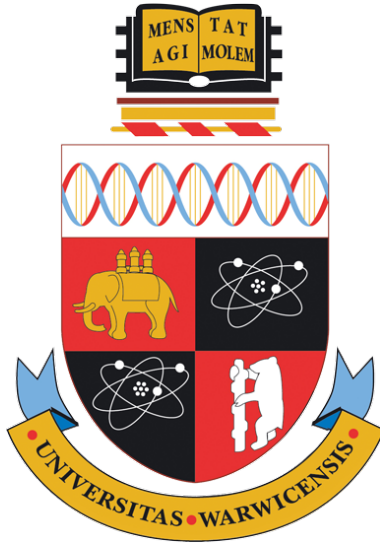
If my thesis does include any substantial subsidiary material owned by third-party copyright holders, I have sought and obtained permission to include it in any version of my thesis available in digital format and that this permission encompasses the rights that I have granted to the University of Warwick and to the British Library.

5. LEGAL INFRINGEMENTS

I understand that neither the University of Warwick nor the British Library have any obligation to take legal action on behalf of myself, or other rights holders, in the event of infringement of intellectual property rights, breach of contract or of any other right, in the thesis.

Please sign this agreement and ensure it is bound into the final hard bound copy of your thesis, which should be submitted to the Library.

Student's signature: Date:



Particle-in-cell simulations of stimulated Raman scattering in the kinetic regime for direct-drive inertial confinement fusion

by

SJ Spencer

Thesis

Submitted to the University of Warwick

in partial fulfilment of the requirements

for admission to the degree of

Doctor of Philosophy

Department of Physics

September 2021

Contents

List of Tables	iv
List of Figures	v
Acknowledgments	viii
Declarations	ix
Abstract	x
Acronyms	xii
Chapter 1 Introduction	1
1.1 Inertial Confinement Fusion	1
1.1.1 Direct and indirect drive ICF	2
1.1.2 Shock-ignition	3
1.2 Previous work	3
1.2.1 Laser-plasma interactions in shock-ignition	3
1.2.2 Simulations	3
1.2.3 Experiments	4
1.2.4 Why PIC in this thesis?	4
1.3 Thesis Outline	4
Chapter 2 Theory	6
2.1 Pre-requisites	6
2.2 The basics: three-wave parametric instabilities	8
2.2.1 Dispersion curves and linear modes	8
2.2.2 Landau damping	9
2.2.3 Stimulated Raman scattering	9
2.2.4 Stimulated Brillouin scattering	10
2.3 Non-linear effects	10
2.3.1 Nonlinear frequency shift	10
2.3.2 Nonlinear Landau damping	10
2.4 Autoresonance	10

Chapter 3 Methods	11
3.1 The particle-in-cell method	11
3.1.1 Field solver	11
3.1.2 Interpolation to particles	12
3.1.3 Particle push	12
3.1.4 Interpolation to the grid	13
3.1.5 EPOCH	13
3.2 EPOCH benchmarking	14
3.2.1 Dispersion relations	14
3.2.2 Linear growth rates	14
3.3 Diagnostics	14
3.3.1 Frequency-filtered diagnostics	14
3.3.2 Auto-resonance diagnostic	14
3.3.3 Inflation threshold diagnostic	14
Chapter 4 Inflationary stimulated Raman scattering in shock-ignition plasmas	16
4.1 Motivation and literature review	16
4.1.1 Homogeneous plasmas	16
4.1.2 Inhomogeneous plasmas	17
4.2 Code and initial conditions	18
4.3 Diagnosing iSRS in inhomogeneous plasmas	20
4.3.1 Inflation threshold	20
4.3.2 Electron trapping	22
4.3.3 Nonlinear frequency shift	23
4.3.4 Beam acoustic modes	24
4.4 Intensity threshold and hot electron scaling	25
4.5 Saturation	27
4.6 Conclusion	28
Chapter 5 Effects of laser bandwidth on inflationary stimulated Raman scattering	32
5.1 Motivation and literature review	32
5.1.1 Absolute SRS	33
5.1.2 Fluid convective SRS	34
5.1.3 Inflationary SRS	35
5.1.4 Multi-beam SRS	35
5.2 Decoupled broadband lasers	36
5.2.1 Conclusions	36
5.3 Realistic laser bandwidth	37
5.4 351nm Nd : glass laser	38

5.4.1	Base case: $\Delta f = 0$	38
5.4.2	SSD-type bandwidth: $\Delta f = 1\text{THz}$	38
5.4.3	Optical parametric amplification: $\Delta f = 10\text{THz}$	39
5.5	248nm krypton fluoride	39
5.5.1	Base case: $\Delta f = 0$	39
5.5.2	Intrinsic bandwidth: $\Delta f = 1, 2, 3 \text{ THz}$	39
5.5.3	Self phase modulation: $\Delta f = 4, 5, 6 \text{ THz}$	39
5.6	193nm argon fluoride	39
5.6.1	Base case: $\Delta f = 0$	40
5.6.2	Intrinsic bandwidth: $\Delta f = 5, 8, 10 \text{ THz}$	40
5.7	Conclusion	40
Chapter 6 Effects of an External Magnetic Field on Stimulated Raman Scattering		41
6.1	Motivation and literature review	41
6.1.1	Magnetic field suppresses kinetic SRS	42
6.1.2	Magnetic field could enhance kinetic SRS	42
6.1.3	What about fluid SRS?	42
6.2	Modelling SRS on LULI	42
6.2.1	Experimental results	42
6.2.2	Simulation results	42
6.3	Magnetic field effect varies with plasma debye length	42
6.3.1	Fixed ions: vary $k_{EPW}\lambda_D$	43
6.4	Magnetic field effect changes with polarisation	43
Chapter 7 Conclusions and Future Work		45
7.1	Conclusion	45
7.1.1	Does any of this matter?	45
7.2	Future Work	45
7.3	Summary	45
Appendix A License Agreements		46

List of Tables

4.1	Summary of density profiles and $k_{EPW}\lambda_D$ values in each simulation. $L_n = n_e/(dn_e/dx)$ evaluated at n_{mid} . For all but the case centred at 0.2 n_{cr} , $k_{EPW}\lambda_D > 0.28$ and we are in the strongly kinetic regime. The total range of $k_{EPW}\lambda_D$ probed is 0.21-0.41.	19
5.1	Laser parameters for this investigation. Where multiple values are pre- sented in a list, each represents a different simulation. The incident laser intensity is set to be approximately the threshold intensity for inflationary SRS. The choice of bandwidths and their implementations in EPOCH are explained and referenced in Sections 5.4, 5.5, 5.6, for the 351, 248, 193 nm cases respectively.	37
5.2	Table shows plasma parameters from simulations performed at the NRL, chosen such that $k_{EPW}\lambda_D$ is between 0.3 and 0.45. The temperature given is the maximum temperature of the particles initialised at $t = 0$, as there is, in reality, a slight temperature gradient in the electron profile. .	37
6.1	T_i is $T_e/3$ in all cases	43
6.2	Plasma density, $k_{EPW}\lambda_D$, regime, predicted behaviour	44

List of Figures

1.1	Thermal reactivity (product of interaction cross-section and velocity averaged over a Maxwellian) as a function of temperature: for deuterium-tritium, deuterium-deuterium (both interaction branches), and deuterium-helium nuclear reactions. Re-printed from https://commons.wikimedia.org/wiki/File:Fusion_rxnrate.svg under a Creative Commons 2.5 license, via Wikimedia Commons.	2
1.2	Shock-ignition design for the National Ignition Facility (NIF) Reprinted with permission from [Perkins et al., 2009]. (all licenses are in Appendices)	3
2.1	Example of autoresonant growth in an EPOCH simulation with parameters: $n_{min} = 0.06n_{crit}$; $n_{max} = 0.17n_{crit}$; $T_e = 4.5\text{keV}$; nPPC = 10,000; $I_0 = 2 \times 10^{15}\text{W/cm}^2$. Black dashed line comes from Chapman <i>et al.</i> [Chapman et al., 2012] formula.	10
4.1	Time-averaged intensity of SRS scattered light for a homogeneous simulation ($n_e = 0.15n_{cr}$, $T_e = 4.5\text{keV}$) with different numbers of particles per cell. Relative errors are given by one standard deviation of the SRS scattered light intensity as calculated from ten simulations.	19
4.2	Blue triangular markers show the intensity of SRS scattered light calculated using the fully-kinetic EPOCH code for parameters: $L_n = 500\mu\text{m}$ and $n_{mid} = 0.15n_{cr}$. Red circular markers show the intensity of SRS scattered light calculated, for the same plasma parameters, from the fluid model presented above. The initial noise level in the fluid model was calculated from a PIC simulation without the laser driver: $I_{noise} = \langle E_y B_z \rangle_{x,t} / \mu_0 = 8 \times 10^{10}\text{W/cm}^2$	21

4.3	Time-resolved comparison of SRS-reflectivity (a,c) and electron distribution functions (b,d) for two simulations with parameters: $L_n = 500\mu\text{m}$; centred at $0.15n_{\text{cr}}$; and $T_e = 4.5\text{keV}$. The distribution function of electron momentum is averaged over the entire spatial domain at four times, normalised to the initial thermal momentum. Panels (a,b) have an incident laser intensity below the threshold for inflationary SRS; $I_0 = 1.13 \times 10^{15}\text{W/cm}^2$. Panels (c,d) have an incident laser intensity above the iSRS threshold; $I_0 = 4.83 \times 10^{15}\text{W/cm}^2$	22
4.4	Top panels show the spectra of electrostatic (a) and electromagnetic (b) waves over the period $0 - 0.7\text{ps}$. The white (orange) dashed lines represent the linear predictions for the spectra of backward (forward) SRS. The bottom panels show the same spectra calculated over the period $1.5 - 1.9\text{ps}$. The E_x (B_z) spectrum is significantly down-shifted (up-shifted), demonstrating a trapped population of electrons in the EPW [Yin et al., 2006]. The orange solid line represents the plasma frequency ω_{pe} for the simulation parameters: $L_n = 500\mu\text{m}$ centred at $0.15n_{\text{cr}}$ and $I_0 = 4.83 \times 10^{15}\text{W/cm}^2$	23
4.5	(a) 2D FFT of E_x over the period $0 - 0.8\text{ps}$. (b) 2D FFT of E_x over the period $1.2 - 1.9\text{ps}$. The white dashed lines represent the analytical dispersion relations corresponding to the minimum (bottom line) and maximum (top line) plasma densities, assuming a Maxwellian electron distribution. The pink dashed line shows the Stokes line for down-shifted EM waves. Simulation parameters: $L_n = 500\mu\text{m}$ centred at $0.15n_{\text{cr}}$ and $I_0 = 4.83 \times 10^{15}\text{W/cm}^2$	24
4.6	(a) Relationship between incident laser intensity and the intensity of SRS scattered light for three different density scale-lengths, with plasma density profiles centred at $0.15n_{\text{cr}}$. (b) Relationship between incident laser intensity and the intensity of SRS scattered light for three simulations with $L_n = 500\mu\text{m}$ centred at three different densities. Each coloured dashed line represents the prediction of the fluid model presented in Section 4.3 for the same parameters as the solid line of the same colour.	26
4.7	(a) Hot electron flux through the right boundary in three simulations with parameters: $I_0 = 2.98 \times 10^{15}\text{W/cm}^2$; $n_{\text{mid}} = 0.15n_{\text{cr}}$; $L_n = 300, 500, 1000\mu\text{m}$. (b) Hot electron flux through the right boundary in three simulations with parameters: $I_0 = 6.16 \times 10^{15}\text{W/cm}^2$; $L_n = 500\mu\text{m}$; $n_{\text{mid}} = 0.12, 0.15, 0.20n_{\text{cr}}$ respectively. Each distribution is normalised to its maximum value. The smooth black line corresponds to the equivalent flux for a Maxwellian distribution with $T_e = 4.5\text{keV}$, for comparison with the bulk plasma.	30

4.8	(a) Poynting flux of scattered light (b) laser energy, showing significant depletion of the pump. Simulation parameters: $L_n = 500\mu\text{m}$ centred at $0.15n_{\text{cr}}$ and $I_0 = 7.83 \times 10^{15}\text{W/cm}^2$	31
5.1	Intensity of light scattered by SRS, averaged over the last three picoseconds of each simulation, for three laser set-ups with fixed maximum normalised chirp ($\Delta\omega\omega_m/\omega_0 = 5.5 \times 10^{-6}$) and varied bandwidth. The simulation parameters common to all data-points are: $T_e = 4\text{keV}$; $L_n = 400\mu\text{m}$; $n_e(x) = 0.11n_{\text{cr}}\exp(x/L_n)$; PPC=16,000.	36
5.2	Intensity of light scattered by backward SRS, time-averaged for all $t > 2\text{ps}$. The incident laser intensity varies between $4 \times 10^{14}\text{W/cm}^2$ and $4 \times 10^{15}\text{W/cm}^2$	38
5.3	placeholder figure for Nd glass sim results	39
5.4	placeholder figure for ArF sim results	40
6.1	cf 0T (left) and 30T (right)	42
6.2	Figure produced by M. Bailly-Grandvaux. Experimentally-measured SRS energy at different gas jet pressures, with and without magnetic fields. The solid-coloured markers represent shots with the laser horizontally polarised with respect to the applied magnetic field, so that the laser magnetic field and applied magnetic field are parallel. The un-filled markers represent vertical polarisation of the laser.	43
6.3	MAthieu made this	44
6.4	I made this. Parameters constant to all sims: $\lambda_0 = 1056\text{nm}$; $L_x = 1000\mu\text{m}$; $T_e = 1\text{keV}$; $I_0 = 1 \times 10^{15}\text{W/cm}^2$; $T_{\text{end}} = 10\text{ps}$; 1000 PPC.	44

Acknowledgments

Thank people here

Declarations

This thesis is submitted to the University of Warwick in support of my application for the degree of Doctor of Philosophy. It has been composed by myself and has not been submitted in any previous application for any degree.

The work presented (including data generated and data analysis) was carried out by the author except in the cases outlined below:

- Figure 6.2 was produced by M. Bailly-Grandvaux (UCSD). It is based on an experiment performed on the LULI laser system by: J. R. Marquès, P. Loiseau, J. Béard, A. Castan, B. Coleman, T. Gangolf, L. Lancia, A. Soloviev, O. Portugall, and J. Fuchs.

Parts of this thesis have been previously published by the author in the following:

- S. J. Spencer, A. G. Seaton, T. Goffrey, and T. D. Arber. Inflationary stimulated Raman scattering in shock-ignition plasmas. *Physics of Plasmas*, 27(12):122705, 2020. doi: 10.1063/5.0022901. URL <https://doi.org/10.1063/5.0022901>

The following research was performed in collaboration during the development of this thesis, but does not form part of the thesis:

- A. Higginson, S. Zhang, M. Bailly-Grandvaux, C. McGuffey, K. Bhutwala, B. J. Winjum, J. Strehlow, B. Edghill, M. Dozieres, F. S. Tsung, R. Lee, S. Andrews, S. J. Spencer, N. Lemos, F. Albert, P. King, M. S. Wei, W. B. Mori, M. J.-E Manuel, and F. N. Beg. Electron acceleration at oblique angles via stimulated raman scattering at laser irradiance $> 10^{16} \text{Wcm}^{-2}\mu\text{m}^2$. *Phys. Rev. E*, 103:033203, Mar 2021. doi: 10.1103/PhysRevE.103.033203. URL <https://link.aps.org/doi/10.1103/PhysRevE.103.033203>
- M. E. Dieckmann, S. J. Spencer, M. Falk, and G. Rowlands. Preferential acceleration of positrons by a filamentation instability between an electron–proton beam and a pair plasma beam. *Physics of Plasmas*, 27(12):122102, 2020. doi: 10.1063/5.0021257. URL <https://doi.org/10.1063/5.0021257>

Where figures have been reprinted from other publications, the re-use license appears in Appendix A.

Abstract

Abstract of max 300 words and max 1 page

Acronyms

DBL	Decoupled broadband laser
DT	Deuterium-Tritium
EPW	Electron plasma wave
ICF	Inertial confinement fusion
ISI	Induced spatial incoherence
iSRS	Inflationary stimulated Raman scattering
LDD	Laser direct-drive
LDI	Langmuir decay instability
LID	Laser indirect-drive
LMJ	Laser Mégajoule
LPI	Laser-plasma interaction
LULI	Laboratoire pour l'Utilisation des Lasers Intenses
NIF	National Ignition Facility
PIC	Particle-in-Cell
SBS	Stimulated Brillouin scattering
SI	Shock ignition
SRS	Stimulated Raman scattering
SSD	Smoothing by spectral dispersion
TPMI	Trapped particle modulation instability

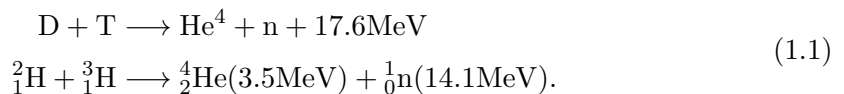
Chapter 1

Introduction

The material presented in this thesis represents kinetic simulations of laser-plasma interactions (LPI) relevant to direct-drive inertial confinement fusion (ICF). In this introductory chapter, an overview of the goals of, and approaches to, inertial confinement fusion is given; including specific details of the ‘shock-ignition’ (SI) ICF scheme. We then review the previous work concerning laser-plasma interactions in direct-drive ICF, and motivate the use of kinetic modelling throughout this thesis. Finally, we offer an outline of the rest of the thesis.

1.1 Inertial Confinement Fusion

The basic concept of inertial confinement fusion (ICF) is based on the Ulam-Teller design for a thermonuclear weapon (H-bomb), which uses radiation to compress thermonuclear fuel to the point where it undergoes nuclear fusion [[Carpintero-Santamaría and Velarde, 2015](#)]. Nuclear fusion is the process by which two light atomic nuclei overcome to electric repulsion between them and combine to form a new, heavier, nucleus and release energy proportional to the mass gap as kinetic energy of the fusion products. The reaction of choice in the thermonuclear weapon, and in most modern ICF designs, is deuterium-tritium (DT) fusion. Equation 1.1 shows the DT reaction; first in the most commonly-presented formula, and then explicitly in terms of the ions and their neutron (superscript) and proton (subscript) numbers.



In order for a fusion reaction to be usable on earth, we require that it satisfies certain criteria: uses the lightest possible elements; reaction occurs at ‘reasonable’ temperatures (on the order of 10keV); reactants (fuel) are obtainable. Figure 1.1 shows that the DT reaction has the largest cross section / highest thermal reactivity of the several reactions which satisfy the above conditions.

In a thermonuclear weapon the radiation source is a fission bomb (also known as

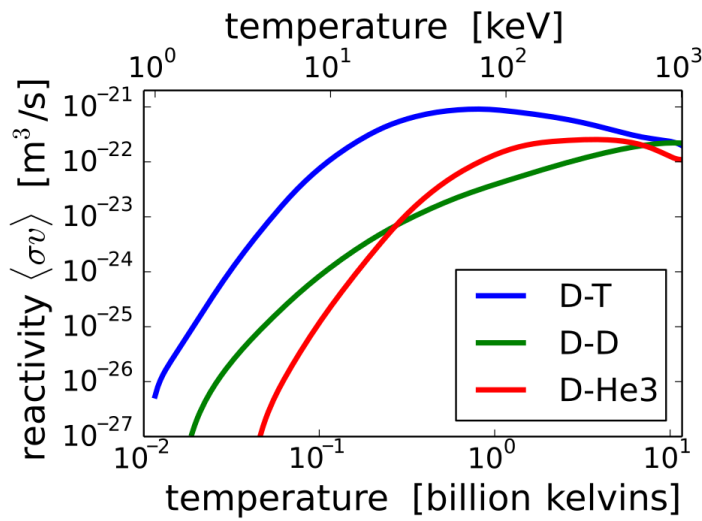


Figure 1.1: Thermal reactivity (product of interaction cross-section and velocity averaged over a Maxwellian) as a function of temperature: for deuterium-tritium, deuterium-deuterium (both interaction branches), and deuterium-helium nuclear reactions. Reprinted from https://commons.wikimedia.org/wiki/File:Fusion_rxnrate.svg under a Creative Commons 2.5 license, via Wikimedia Commons.

an ‘atom bomb’ or ‘A-bomb’), which detonates and reaches very high temperatures, producing thermal x-rays which are channelled to compress the thermonuclear fuel. The fusion reaction which results from the high density and temperature conditions created in the compressed fuel is unconfined and, therefore, unsuited for energy generation. When lasers were proposed and realised, by Schawlow and Townes [1958] and Maiman [1960] respectively, scientists at Lawrence Livermore National Laboratory realised that lasers had the potential to ignite fusion explosions without using an atomic bomb. In 1972, Nuckolls et al. [1972] published a paper in Nature in which they used the LASNIX computer code to show that high-energy lasers could be used to compress hydrogen to super-high densities. Combined with small target pellets of fusion fuel, which will undergo burn before exploding (due to their inertia), the basic idea of inertial-confinement fusion was born. We now know that ICF was demonstrated successfully in underground nuclear tests, just ten years after Nuckolls proposed it, but with a fission bomb as the driver, rather than a laser [Evans, 2010].

1.1.1 Direct and indirect drive ICF

Developments on the basic ICF scheme can be categorised by how the laser is used to perform the radiation compression of the fuel. In laser indirect-drive (LID) models, fusion fuel is held inside a hollow chamber made of a high atomic number material. This structure is known as the hohlraum, from the German for ‘hollow space’. Lasers are then used to heat the inside walls of the hohlraum until they emit a bath of X-rays which heat

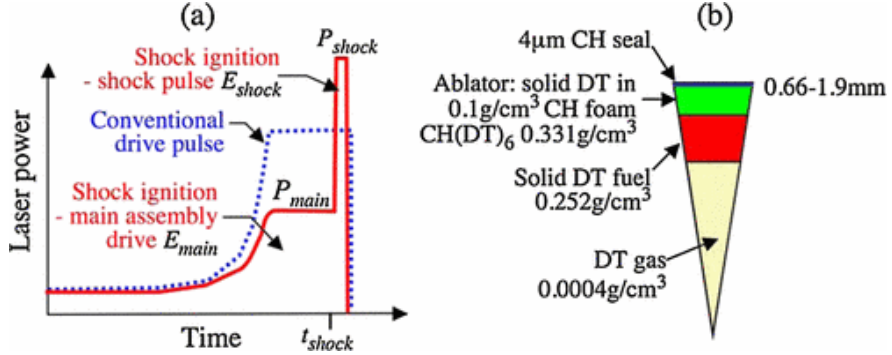


Figure 1.2: Shock-ignition design for the National Ignition Facility (NIF) Reprinted with permission from [Perkins et al., 2009]. (all licenses are in Appendices)

the outer layer of the fuel capsule, causing the outer layer of the capsule to ablate and a rocket-effect-like implosion of the inner fuel. It is clear that this process is very similar to the indirect approach used to drive the thermonuclear explosion in the Ulam-Teller design. As such, the National Ignition Facility (NIF) (US) and Laser Mégajoule (LMJ) (France) are set-up for indirect-drive ICF, in order to support their respective country's nuclear weapons research programmes. An advantage of the indirect-drive technique is that the absorption and re-emission of laser energy by the hohlraum smooths the radiation which will drive the implosion.

Improvements in laser smoothing technology have made this advantage of LID less obvious, and much research now focuses on laser direct-drive (LDD). In laser direct-drive the laser beams are aimed at the target directly. Go through the steps: ablation; shocks; shocks; ignition. One limit to the success of any direct-drive scheme is the direct interaction of the laser with the coronal plasma.

1.1.2 Shock-ignition

This is a directly-driven central ignition scheme boosted by a strong shock.

1.2 Previous work

1.2.1 Laser-plasma interactions in shock-ignition

1.2.2 Simulations

Kinetic models

Fluid models with kinetic effects

Basically it's interesting that you can put some of these effects into a fluid model, such as here [Tran et al., 2020]

1.2.3 Experiments

1.2.4 Why PIC in this thesis?

Question: doesn't PIC suck for predicting experimental observables?

Need kinetics. Too expensive to use VFP for these laser-plasma interactions since the WFP velocity grid must be fine enough to resolve the electron quiver velocity. Also we have a PIC code in-house.

1.3 Thesis Outline

In the next five chapters, the wokr h uhuihuh uhi

Chapter 2 We present in Chapter 2 the theory of laser-plasma interactions relevant to this thesis. We derive,... blah is introduced ... We describe the basic linear, quasi-linear, and non-linear theory required to understand normal modes; wave-particle interactions; and wave-wave instabilities, respectively, which are relevant to the coronal plasmas in direct-drive ICF.

Chapter 3 Here we present the EPOCH particle-in-cell (PIC) code, which is used to perform all the simulations presented in this thesis, alongside a review of the PIC method for kinetic plasma simulations. Basic benchmarking of the code to the theory presented in Chapter 2 is performed, and we introduce several key diagnostics which are used throughout the thesis.

Chapter 4 In this work, we use one-dimensional particle-in-cell simulations to show that there is a non-linear frequency shift caused by kinetic effects, resulting in the growth of SRS in an inhomogeneous plasma far exceeding the predictions of fluid theory, so-called inflationary SRS or iSRS. We find that iSRS occurs over a wide range of density scale-lengths relevant to shock-ignition and other directly- driven inertial confinement fusion schemes. Here we quantify the intensity threshold for the onset of iSRS for shock-ignition relevant parameters.

Chapter 5 In this chapter, results of one-dimensional PIC simulations are presented, which represent the first investigation into the practical possibility of using broadband to suppress inflationary SRS in shock-ignition. We show that for a decoupled broadband laser, the non-linear frequency shift must be taken into account when calculating the condition for suppression of iSRS. Next we consider the case of realistic shock-ignition schemes on three laser systems: frequency-tripled Nd : glass; Krypton Fluoride (KrF); and Argon Fluoride (ArF).

Chapter 6 Here we present

Conventions adopted in the thesis

Unless otherwise stated in the text, all equations and physical quantities in this thesis are in SI units. Standard SI prefixes (k for kilo, T for tera- etc) are used. All numerically-calculated values are given to two significant figures, and written in scientific notation for values greater than 1000, and less than 1/1000.

Chapter 2

Theory

This chapter aims to equip the reader with the tools they need to read, and to engage critically with, the rest of the thesis. By the end of this chapter, the reader should be familiar with the following concepts and methods:

1. Stimulated Raman scattering (SRS) as a three-wave parametric instability.
2. The difference between convective and absolute SRS, and how we can quantify their gain.
3. The difference between fluid and kinetic SRS, and how we can use $k_{\text{EPW}}\lambda_D$ to delineate these two regimes.
4. The effect of large trapped-particle populations on SRS, including the growth of additional resonant modes.

2.1 Pre-requisites

This section provides a minimal set of pre-requisites I will be assuming in this chapter. First up, we have Maxwell's equations in differential form:

$$\nabla \times \vec{E} = -\frac{\partial \vec{B}}{\partial t} \quad (\text{Faraday-Lenz Law}) \quad (2.1)$$

$$\nabla \times \vec{B} = \mu_0 \vec{j} + \frac{1}{c^2} \frac{\partial \vec{E}}{\partial t} \quad (\text{Ampere-Maxwell Law}) \quad (2.2)$$

$$\nabla \cdot \vec{B} = 0 \quad (\text{No Magnetic Monopoles}) \quad (2.3)$$

$$\nabla \cdot \vec{E} = \frac{\rho}{\epsilon_0} \quad (\text{Gauss's Law}). \quad (2.4)$$

These describe the evolution of the vector fields $[\vec{E}(\vec{x}, t), \vec{B}(\vec{x}, t)]$ using the mathematical notation $\nabla = \left(\frac{\partial}{\partial x}, \frac{\partial}{\partial y}, \frac{\partial}{\partial z} \right)$ to denote the scalar function divergence ($\nabla \cdot$) and the vector

function curl ($\nabla \times$). The charge density ρ and current density \vec{j} are most properly calculated by summing the contributions of the exact phase-space coordinates of every particle in the plasma. However, we can make an approximation and assume that the phase space is continuous and take an average to get the distribution function $f(\vec{x}, \vec{v}, t)$. We can now define ρ and \vec{j} in terms of the distribution function like so:

$$\rho = q \int d\vec{v} f(\vec{x}, \vec{v}, t) \quad (2.5)$$

$$\vec{j} = q \int d\vec{v} \vec{v} f(\vec{x}, \vec{v}, t). \quad (2.6)$$

In order to close the Maxwell equations, we need an equation which tells us how the distribution function evolves in terms of $[\vec{E}(\vec{x}, t), \vec{B}(\vec{x}, t)]$. An entire two weeks of kinetic theory lectures later, we end up with the Vlasov equation for a collisionless plasma:

$$\frac{\partial f}{\partial t} + \vec{v} \cdot \nabla f + \frac{q}{m} \left(\vec{E} + \frac{\vec{v} \times \vec{B}}{c} \right) \cdot \frac{\partial f}{\partial \vec{v}} = 0 \quad (2.7)$$

By taking moments of the Vlasov equation (and moving to 1D for brevity), we obtain the following reduced description of the plasma in terms of a fluid of electrons:

$$\frac{\partial n}{\partial t} + \frac{\partial}{\partial x}(nu) = 0 \quad (\text{0th moment: Continuity equation}) \quad (2.8)$$

$$m_e n \left(\frac{\partial u}{\partial t} + u \frac{\partial}{\partial x} u \right) = -\frac{\partial P}{\partial x} + q E_x n \quad (\text{1st moment: Momentum equation}). \quad (2.9)$$

Where n is the number density (calculated by taking the zeroth moment of the distribution function); u is the macroscopic flow velocity (calculated by taking the first moment of the distribution function); and P is a scalar pressure. In order to close this set of equations, we require an expression for the scalar pressure P that does not introduce any higher moments of the distribution function. Typically in this thesis the timescales are such that thermal conduction can be neglected, and we assume that the process is adiabatic. This means that our final equation takes the form:

$$\frac{d}{dt} \left(\frac{P}{n^\gamma} \right) = 0, \quad (2.10)$$

with $\gamma = C_p/C_v = (n+2)/2 = 3$ in one dimension.

We must also recall the fundamental time and length scales associated with a plasma: the plasma frequency and the Debye length. The plasma frequency describes the natural frequency of oscillation of (generally) electrons in a cold plasma, its expression in terms of the electron number density can be derived by considering the displacement of a

block of plasma and considering the restoring forces, to give:

$$\omega_{pe} = \sqrt{\frac{n_e e^2}{m_e \epsilon_0}}. \quad (2.11)$$

This fundamental time-scale allows us to define a fundamental length-scale based on how far a particle with thermal velocity v_{th} can travel in one oscillation period.

$$\lambda_D = \frac{v_{th}}{\omega_{pe}} \propto \left(\frac{\text{temperature}}{\text{density}} \right)^{1/2}. \quad (2.12)$$

2.2 The basics: three-wave parametric instabilities

Equipped with this brief revision of the fundamental relationships which describe a plasma, we can now move onto the theory behind our object of study: stimulated Raman scattering.

2.2.1 Dispersion curves and linear modes

One obvious thing to do, now that we have the fluid equations for an electron plasma, would be to look for normal modes of the system. These describe oscillations in which all variables vary sinusoidally with the same frequency, meaning that they can be written as $n(x, t) = n_1(x)\exp(-i\omega t)$. A non-magnetised, two-species (electron-ion) plasma supports two electrostatic (no time-varying magnetic fields) modes and one electromagnetic mode.

$$\omega^2 = \omega_{pe}^2 + 3k^2 v_{th}^2 \quad (\text{Electron plasma wave}) \quad (2.13)$$

$$\omega = c_{si} k \quad (\text{Ion acoustic wave}) \quad (2.14)$$

$$\omega^2 = \omega_{pe}^2 + c^2 k^2 \quad (\text{Electromagnetic wave}) \quad (2.15)$$

With these three waves, we find the following three-wave parametric instabilities:

EMW1 → EPW + EMW2	(Stimulated Raman Scattering)
EMW1 → IAW + EMW2	(Stimulated Brillouin Scattering)
EMW1 → EPW1 + EPW2	(Two-Plasmon Decay)
EPW1 → EPW2 + IAW	(Langmuir Decay Instability)
EMW → EPW + IAW	(The Parametric Instability)

2.2.2 Landau damping

Unfortunately, by looking for normal modes, we have forced ourselves to find normal modes and we have ignored the possibility of damped oscillations in the system. Considering the electron plasma wave as an initial value problem

2.2.3 Stimulated Raman scattering

Rosenbluth gain

Since the instability we are concerned with is convective, we would like to understand what the maximum wave amplitude is for the daughter waves, according to the linear theory, in order to determine how SRS will grow in the fluid regime.

The derivation below follows the steps laid out in [Nishikawa and Liu \[1976\]](#), with the following adaptations for this thesis: some steps written out in more explicit detail; notation changes, to improve the readability; and minor typographical corrections.

We use our physical understanding of the system to make the following assumptions:

1. undamped EMW $\Gamma_1 = 0$
2. strong damping and slow convection of EPW
3. constant source at 0, maximum value at $+\infty$
4. perfect matching at $x = 0$, assume κ is well-approximated by $\kappa(x) = \kappa'(0)x$.

Consider a three-wave parametric instability that takes place in a plasma slab with a density gradient in x with a uniform pump. The density gradient leads to x -varying wavenumbers for the waves, so we define the ‘wavenumber mismatch’ as $\kappa = k_0(x) - k_1(x) - k_2(x)$, where perfect matching is defined by the condition $\kappa(x = 0) = 0$ and we insist that $\kappa = \kappa'x$. The daughter waves can be described by the following pair of partial differential equations:

$$\left(\frac{\partial}{\partial t} + v_1 \frac{\partial}{\partial x} + \Gamma_1 \right) a_1 = \gamma_0 a_2 \exp\left(\frac{i\kappa' x^2}{2}\right) \quad (2.16)$$

$$\left(\frac{\partial}{\partial t} + v_2 \frac{\partial}{\partial x} + \Gamma_2 \right) a_2 = \gamma_0 a_1 \exp\left(\frac{-i\kappa' x^2}{2}\right); \quad (2.17)$$

where $\Gamma_{1,2}$ are the damping rates; $a_{1,2}$ the action amplitudes; and $v_{1,2}$ the group velocities of the two waves.

WHAT ARE WE TRYING TO DO, WHAT MOTIVATES THIS TRANSFORM?

Recalling the definition of the Laplace transform of a function $f(t)$: $L\{f(t)\} = F(p) = \int_0^\infty e^{-pt} f(t) dt$ we take the Laplace transform of these equations to get

2.2.4 Stimulated Brillouin scattering

2.3 Non-linear effects

A key aspect of quasilinear theory is its identification of the distinction between resonant and non-resonant particles, scattering and diffusion [Sagdeev and Diamond, 2018].

2.3.1 Nonlinear frequency shift

non-linear basis for trapping induced SRS modes found in Rose and Russell [2001]

2.3.2 Nonlinear Landau damping

2.4 Autoresonance

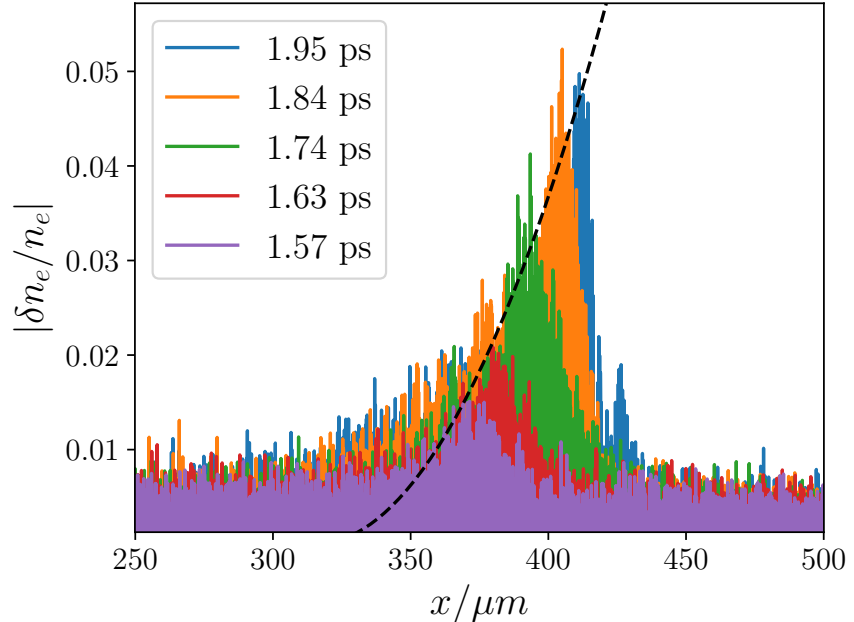


Figure 2.1: Example of autoresonant growth in an EPOCH simulation with parameters: $n_{min} = 0.06n_{crit}$; $n_{max} = 0.17n_{crit}$; $T_e = 4.5\text{keV}$; nPPC = 10,000; $I_0 = 2 \times 10^{15}\text{W/cm}^2$. Black dashed line comes from Chapman *et al.* [Chapman et al., 2012] formula.

Chapter 3

Methods

3.1 The particle-in-cell method

The core components of a PIC code are: a fixed spatial grid; a solver that moves charged particles according to the Lorentz force law and calculates currents due to this motion (the particle pusher); and a solver which uses the calculated currents to solve Maxwell's equations on the grid (the field solver) [Arber et al., 2015]. There are three fundamental features of a PIC code which make it ontologically different from a true plasma: firstly, time is discrete rather than continuous; secondly, electromagnetic fields only take well-defined values on a discrete spatial grid; and thirdly, simulation pseudo-particles have a non-zero size and shape. These are computational limitations, but also practical considerations which make the mathematics behind the simulation more tractable.

3.1.1 Field solver

The key point of a PIC simulation is that the system evolves *self-consistently*, this means that every time the particles move we must calculate the electric and magnetic fields generated by their new charge and current densities. To calculate these new fields we need to solve Maxwell's equations:

$$\begin{aligned}\nabla \times \mathbf{E} &= -\frac{\partial}{\partial t} \mathbf{B} \\ \nabla \times \mathbf{B} &= \mu_0 \left(\mathbf{j} + \epsilon_0 \frac{\partial}{\partial t} \mathbf{E} \right) \\ \nabla \cdot \mathbf{B} &= 0 \\ \nabla \cdot \mathbf{E} &= \frac{\rho}{\epsilon_0}\end{aligned}\tag{3.1}$$

where ρ and \mathbf{j} are the charge and current densities respectively, which have been calculated as part of the particle pusher. These are differential equations, which means we can solve them by some sort of finite-difference method, in which the full and partial differentials are replaced by difference equations (we saw this already in the construction

of the particle pusher). The system can be simplified by realising that, since we will be solving at a discrete time step, $\partial\mathbf{B}/\partial t = \partial\mathbf{E}/\partial t = 0$. This reduces the system to be solved to a single equation:

$$\nabla^2\phi = -\frac{\rho}{\epsilon_0} \quad (3.2)$$

which is then solved by taking Fourier transforms of ρ and ϕ . The Fourier transform is a generalisation of the complex Fourier series when the length of the function domain tends to infinity [Weisstein]. The Fourier transform is often thought of as a transformation between a function in the space-domain and the same function in the frequency-domain. As such, it can be defined by the functor \mathcal{F}_x defined by

$$\begin{aligned} F(k) &= \mathcal{F}_x[f(x)](k) \\ &= \int_{-\infty}^{\infty} f(x)e^{-2\pi ikx}dx. \end{aligned} \quad (3.3)$$

The Fourier transform transforms ∇^2 to k^2 , which makes Equation 3.2

$$\phi(k) = \frac{\rho(k)}{\epsilon_0 k^2}, \quad (3.4)$$

this is an explicit expression for $\phi(k)$ in terms of known quantities. We can now use the inverse Fourier transform to calculate $\phi(x)$ and $\mathbf{E}(x)$ like so [Birdsall and Langdon, 1991]:

$$\rho(x) \xrightarrow{\text{FFT}} \rho(k) \xrightarrow{k^2} \phi(k) \xrightarrow{\text{IFFT}} \phi(x) \xrightarrow{\nabla\phi} \mathbf{E}(x)$$

We now have an expression for \mathbf{E} on the grid, and can find \mathbf{B} by substituting it back into Maxwell's equations. The final step of the field solver in EPOCH is to interpolate from the field values on the grid, to forces at the particle positions.

3.1.2 Interpolation to particles

3.1.3 Particle push

The basic particle pusher acts to integrate the equations of motion for the charged particles and then to accelerate the particles to new velocities, and to translate them to new positions. The equation of motion for charged particles in a plasma comes from the Lorentz force law:

$$m\frac{d\mathbf{v}}{dt} = q(\mathbf{E} + \mathbf{v} \times \mathbf{B}) \quad (3.5)$$

In EPOCH the particle pusher actually solves the full relativistic Lorentz force law, but we will consider the non-relativistic case here for simplicity. Equation 3.5 can be solved by solving the three simultaneous equations which come from time-centering the magnetic term [Birdsall and Langdon, 1991] like so

$$\frac{\mathbf{v}_{t+\Delta t/2} - \mathbf{v}_{t-\Delta t/2}}{\Delta t} = \frac{q}{m} \left[\mathbf{E}_t + \frac{\mathbf{v}_{t+\Delta t/2} + \mathbf{v}_{t-\Delta t/2}}{2} \times \mathbf{B}_t \right]$$

A more elegant solution is to separate solving the magnetic and electric effects on the motion by using the Boris substitution [Birdsall and Langdon, 1991]

$$\mathbf{v}_{t+\Delta t/2} = \mathbf{v}^+ + \frac{q\mathbf{E}_t}{m} \frac{\Delta t}{2} \quad (3.6)$$

$$\mathbf{v}_{t-\Delta t/2} = \mathbf{v}^- - \frac{q\mathbf{E}_t}{m} \frac{\Delta t}{2} \quad (3.7)$$

which gives:

$$\frac{\mathbf{v}^+ - \mathbf{v}^-}{\Delta t} = \frac{q}{2m} (\mathbf{v}^+ + \mathbf{v}^-) \times \mathbf{B}_t. \quad (3.8)$$

The second equation of motion ($\mathbf{v} = d\mathbf{x}/dt$) is solved using the following integrator:

$$\frac{\mathbf{x}_{t+1} - \mathbf{x}_t}{\Delta t} = \mathbf{v}_{t+\Delta t/2}. \quad (3.9)$$

Equations 3.8 and 3.9 together form a second order leapfrog integrator; conventionally understood to be the integrator with the best balance between accuracy, stability and efficiency. The final step of the particle pusher is interpolating from the new particle positions and velocities to new values of the current and charge densities on the grid.

3.1.4 Interpolation to the grid

3.1.5 EPOCH

EPOCH is a collisionless plasma physics simulation code that uses the Particle in Cell (PIC) method to move particles in self-consistently evolving electric and magnetic fields. EPOCH is an MPI parallelised, explicit, second-order, relativistic PIC code which is controlled through a customisable input deck Arber et al. [2015]. The interaction of the user with the EPOCH code is limited to the creation of an input deck for each simulation experiment. This document contains the key simulation parameters, such as: the charge and density of various particle species; background electric and magnetic fields; and the duration of the simulation. The input deck also requires you to choose the sizes of your spatial grid and time step, this is very important as you need to be able to resolve the effect you are studying.

“EPOCH (Extendable PIC Open Collaboration) project. EPOCH is a Birdsall and Langdon (with Villasenor and Buneman charge conservation) type Particle in Cell (PIC) code in 1, 2 and 3D that has been developed at the University of Warwick as the basis for a standard, extendable PIC code. It has been designed for both ease of use and ease of extension with both new physics and new user interface elements. EPOCH is written using standard Fortran95 and MPI and is open source enabling it to be easily modified for specific use cases. The code has seen widespread adoption with several hundred registered users and has become one of the standard PIC codes used by the plasma physics research community.” Keith’s website

3.2 EPOCH benchmarking

3.2.1 Dispersion relations

3.2.2 Linear growth rates

3.3 Diagnostics

The EPOCH code produces outputs in terms of physical variables, for example, electric and magnetic fields as functions of space and time. It can be useful to plot these directly, but also to plot them in terms of frequency and wavenumber. As such

3.3.1 Frequency-filtered diagnostics

3.3.2 Auto-resonance diagnostic

3.3.3 Inflation threshold diagnostic

According to fluid theory, the growth of a parametrically unstable mode in an inhomogeneous plasma is limited by the loss of resonance between the waves as they propagate through the plasma and experience wave-number shift [Rosenbluth \[1972\]](#). We can formulate this inhomogeneous growth in terms of the Rosenbluth gain exponent [Rosenbluth \[1972\]](#)

$$G_{\text{Ros}} = 2\pi\gamma_0^2 / |v_{g,1}v_{g,2}\kappa'|, \quad (3.10)$$

where γ_0 is the growth rate of the equivalent mode in a homogeneous plasma, $v_{g,1}, v_{g,2}$ are the group speeds of the scattered EM wave/EPW and κ' is the x -derivative of the wave-number mismatch $\kappa(x) = k_0(x) - k_s(x) - k_{\text{EPW}}(x)$. The maximum intensity reached by a parametrically unstable wave which has grown from noise at point x is then given by the expression $I_{\text{noise}}\exp(G_{\text{Ros}}(x))$. In order to calculate the intensity of scattered light due to SRS, we substitute for k_0, k_s, k_{EPW} using the electromagnetic and Bohm-Gross dispersion relations in one dimension, to get:

$$\frac{d\kappa}{dx} = -\frac{1}{2} \frac{q_e^2}{m_e \epsilon_0} \left(\frac{1}{c^2 k_0} - \frac{1}{3v_{\text{th}}^2 k_{\text{EPW}}} - \frac{1}{c^2 k_s} \right) \frac{dn_e}{dx}. \quad (3.11)$$

Substituting this back into G_{Ros} with the growth rate for backward SRS in a homogeneous plasma [Kruer \[2003\]](#),

$$\gamma_0 = \frac{k_{\text{EPW}} v_{os}}{4} \left[\frac{\omega_{\text{pe}}^2}{\omega_{\text{EPW}}(\omega_0 - \omega_{\text{EPW}})} \right]^{1/2}, \quad (3.12)$$

gives an appropriate Rosenbluth gain exponent for calculating convective amplification of back-scattered SRS light in our simulations.

We make several simplifying assumptions that allow us to estimate the maximal scattered light intensity at a point in our simulation domain. Firstly, we neglect the

dependence of the scattered light velocity on space, and consider it to be fixed at c . This means that we slightly over-estimate the amount of scattered light which is able to reach the point x in time t . We also assume that the laser achieves its maximum intensity starting at $t = 0$ rather than ramping up, as it does in the simulations. We neglect collisional damping of the scattered EM waves and assume that the noise source I_{noise} is homogeneous in the domain. Finally, we assume that the amplification described by the Rosenbluth gain exponent occurs locally and instantaneously at the point of perfect matching ($\kappa = 0$), rather than across the resonance region defined by $\ell \sim 1/\sqrt{\kappa'}$. For all the simulations presented in this paper $\ell < 6\mu\text{m}$. The scattered light intensity is then given by

$$I(x) = \frac{1}{L_x} \int_x^{L_x} I_{\text{noise}} \exp(G_{\text{Ros}}(s)) ds. \quad (3.13)$$

The prefactor $1/L_x$ ensures that if $G_{\text{Ros}} = 0$, such that there is no growth, then the back-scattered signal remains at the noise intensity. The steady-state intensity of SRS scattered light measured at the laser-entry boundary is then given by $\langle I_{\text{SRS}} \rangle = I(0)$.

Obviously this model is limited to calculating the maximum reflected light ignoring the effects of pump depletion. It is only applicable for these intensities Using the code LPSE might be more realistic, but we don't think it can do convective growth yet. In Han braodband preprint they find the trheshold by fitting some weird function, what do I think of that?

Chapter 4

Inflationary stimulated Raman scattering in shock-ignition plasmas

This chapter is adapted, with the permission of AIP Publishing, from:

- S. J. Spencer, A. G. Seaton, T. Goffrey, and T. D. Arber. Inflationary stimulated Raman scattering in shock-ignition plasmas. *Physics of Plasmas*, 27(12):122705, 2020. doi: 10.1063/5.0022901. URL <https://doi.org/10.1063/5.0022901>.

In this chapter, results of one-dimensional (1D) particle-in-cell simulations are presented, which show that inflationary SRS (iSRS) can occur in shock-ignition plasmas and which characterise its threshold intensity in terms of the density scale length of the coronal plasma. Inflationary SRS refers to the enhancement of SRS above the levels predicted by fluid theory, caused by kinetic effects. The chapter begins with a review of the previous work on inflationary SRS in homogeneous plasmas, where the effect was first identified and understood. Then the case of iSRS in large-scale inhomogeneous plasmas is considered, and a description in terms of autoresonance is presented. The code and initial conditions of the simulation are described, followed by a review of the signatures of iSRS and how they manifest in an inhomogeneous plasma. Finally the dependence of the inflationary SRS threshold intensity on density scale length for shock-ignition parameters, and the saturation of the instability are explored. The conclusion discusses the applicability of these results and ways to increase the experimental relevance of the simulations.

4.1 Motivation and literature review

4.1.1 Homogeneous plasmas

Inflationary SRS has been studied extensively in the low-density homogeneous plasmas relevant to indirect-drive ICF on the NIF [Ellis et al., 2012; Strozzi et al., 2007; Vu

et al., 2002, 2007; Yin et al., 2006, 2008, 2012]. In attempting to explain experimental measurements of large SRS-reflectivities at high values of $k_{EPW}\lambda_D$ [Fernández et al., 2000; Montgomery et al., 2002], it was suggested that some mechanism caused a reduction in the Landau damping rate by four to five times, compared to the damping for a Maxwellian plasma [Montgomery et al., 2002]. Anomalously large SRS-reflectivities were recreated in simulations [Vu et al., 2001, 2002], and were explained by reference to O’Neil’s 1965 model of reduced EPW damping caused by electron-trapping [O’Neil, 1965]. In homogeneous plasmas, iSRS occurs when an SRS EPW grows to a point where it can trap electrons for one complete bounce period or longer, without them becoming de-trapped due to velocity-space diffusion or side-loss [Vu et al., 2002]. This trapped electron population leads to modification of the distribution function, in the form of a locally flattened region around the EPW phase velocity. This translates to a modification of the dielectric properties of the plasma, resulting in a reduction in the EPW’s associated Landau damping rate [O’Neil, 1965; Vu et al., 2002], and increased SRS growth.

Key results of previous studies of inflationary SRS in homogeneous plasmas include: a theory for the saturation of iSRS in terms of EPW bowing and the trapped-particle modulation instability [Yin et al., 2008]; the derivation of an inflation threshold intensity in terms of competition between trapping in the EPW and diffusion in velocity space [Vu et al., 2007]; and the description of iSRS in terms of a transition from convective to absolute growth [Wang et al., 2018]. Inflationary SRS has also been identified as an important mechanism in simulations with ensembles of laser speckles [Winjum et al., 2019; Yin et al., 2012].

4.1.2 Inhomogeneous plasmas

In the large-scale inhomogeneous plasmas associated with shock-ignition ($L_n \simeq 300 - 1000\mu\text{m}$) the mechanism and effects of inflationary SRS have received much less attention. The few papers which do refer to iSRS in SI inhomogeneous plasmas assume that the explanation of iSRS in a homogeneous plasma in terms of reduced Landau damping also applies to iSRS in an inhomogeneous plasma. However, iSRS in an inhomogeneous plasma actually happens by a different mechanism. In the case of a homogeneous plasma, reduced Landau damping due to electron-trapping in the EPW leads to an increase of the SRS growth rate which, if sufficiently large, can cause a transition from convective to absolute growth [Wang et al., 2018]. For an inhomogeneous plasma, where the growth of SRS is always convective, the reduction in Landau damping associated with trapping in the EPW has no net effect on the convective gain [Williams, 1991].

While the local SRS growth rate may depend on the EPW damping rate in an inhomogeneous plasma, the region of SRS convective growth is also extended, leading to a net Rosenbluth gain [Rosenbluth, 1972] which is independent of Landau damping [Liu and Tripathi, 1994; Williams, 1991]. We therefore look to another non-linear

effect caused by the trapped electrons in the SRS EPW, the non-linear frequency shift [Morales and O’Neil, 1972]. In an inhomogeneous plasma, the frequency shift resulting from electron-trapping can compensate for the wave-number mismatch on propagating up the density gradient, thereby allowing growth over a larger region - an auto-resonance [Chapman et al., 2010, 2012]. Chapman et al. [2012] proposed this theory for iSRS in an inhomogeneous ($L_n \lesssim 100\mu\text{m}$) plasma close to the hohlraum wall in indirect-drive ICF. They demonstrated the auto-resonant interaction Chapman et al. [2010] between the non-linear frequency shift associated with electron-trapping in EPW and the wave-number mismatch caused by plasma inhomogeneity; which allows larger SRS gain Chapman et al. [2012].

Inflationary SRS has been suggested as the cause of SRS from low densities in simulations of LPI in shock ignition [Klimo et al., 2014]. Sub-scale shock-ignition experiments have detected SRS scattered light from densities $0.09 - 0.16n_{\text{cr}}$, where the inflationary mechanism should be important [Cristoforetti et al., 2017]. Recent full-scale ($L_n > 500\mu\text{m}$, $T_e = 5\text{keV}$) directly-driven experiments have detected significant SRS-reflected light from densities $0.15 - 0.21n_{\text{cr}}$ [Rosenberg et al., 2020]. Another full-scale ($L_n = 450\mu\text{m}$, $T_e = 4.5\text{keV}$) SI experiment measured SRS-reflected light from densities between $0.05 - 0.15n_{\text{cr}}$. Under the conditions of the experiment, $k_{\text{EPW}}\lambda_D$ ranges from $0.3 - 0.6$ and the measured SRS is assumed to be inflationary in origin [Baton et al., 2020]. For a single laser speckle in an inhomogeneous plasma with density scale-length $L_n \simeq 70\mu\text{m}$, Riconda et al. [2011] demonstrated that iSRS was associated with electron-trapping in the EPW. By varying $a_0 = eE_0/cm_e\omega_0$ from 0.03 to 0.06, i.e. an increase in laser intensity from $1.0 \times 10^{16}\text{W/cm}^2$ to $4 \times 10^{16}\text{W/cm}^2$, they showed a transition to iSRS.

4.2 Code and initial conditions

As described in Chapter 3, all simulations are performed using the EPOCH [Arber et al., 2015] particle-in-cell code. The simulation parameters are chosen to achieve our primary aim of identifying plasma parameters where iSRS may occur; which does not require large simulations of the entire LPI system. The simulations all used a domain size of $L_x = 100\mu\text{m}$ and ran to $T_{\text{end}} = 2\text{ps}$ with 2048 particles per cell (PPC) for the electron species. We treat the ions as a neutralising background population, since we simulate only a two pico-second interval of SRS development, during which ion dynamics will not become important [Rousseaux et al., 2006]. For the plasma parameters laid out above, electron-ion collisions occur on a characteristic timescale of approximately 7ps at the highest density probed, $0.22n_{\text{cr}}$. Since the inflationary Raman process we are investigating takes place on a sub-picosecond timescale, we do not include collisions in our simulations. The plasma density profiles are given by the expression $n(x) = n_{\text{min}}\exp(x/L_n)$ and can be seen in Table 4.1.

We simulate a frequency-tripled Nd:glass laser with vacuum wavelength $\lambda_0 = 351\text{nm}$,

$L_n/\mu\text{m}$	$n_{\text{mid}}/n_{\text{cr}}$	$(n_{\text{min}}, n_{\text{max}})/n_{\text{cr}}$	$(k\lambda_{D_{\text{min}}}, k\lambda_{D_{\text{max}}})$
300	0.15	(0.13, 0.18)	(0.28, 0.37)
500	0.12	(0.11, 0.13)	(0.37, 0.41)
500	0.15	(0.14, 0.17)	(0.29, 0.35)
500	0.20	(0.18, 0.22)	(0.21, 0.27)
1000	0.15	(0.14, 0.16)	(0.31, 0.32)

Table 4.1: Summary of density profiles and $k_{EPW}\lambda_D$ values in each simulation. $L_n = n_e/(dn_e/dx)$ evaluated at n_{mid} . For all but the case centred at $0.2n_{\text{cr}}$, $k_{EPW}\lambda_D > 0.28$ and we are in the strongly kinetic regime. The total range of $k_{EPW}\lambda_D$ probed is 0.21-0.41.

polarised in the y -direction. The laser intensity was varied in 20 logarithmically evenly-spaced increments between 10^{14}W/cm^2 and 10^{16}W/cm^2 , with a half-Gaussian temporal profile followed by a flat top, and a rise-time of 50 laser periods. We use absorbing boundaries for the fields and thermal for the particles; these replace any particle leaving the simulation with an incoming particle with velocity consistent with a Maxwellian plasma based on the initial temperature of 4.5keV.

EPOCH uses a pseudorandom number generator (PRNG) to generate the initial particle distribution. Each simulation was repeated 10 times with a different PRNG seed, allowing us to determine the sensitivity of SRS to plasma fluctuations. This allowed us to calculate both the mean and standard deviation of the intensity of the light scattered through SRS.

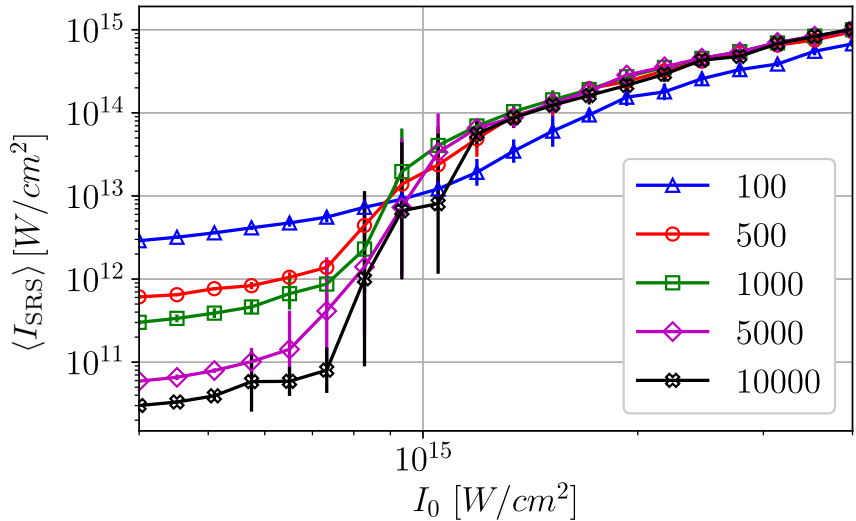


Figure 4.1: Time-averaged intensity of SRS scattered light for a homogeneous simulation ($n_e = 0.15n_{\text{cr}}$, $T_e = 4.5\text{keV}$) with different numbers of particles per cell. Relative errors are given by one standard deviation of the SRS scattered light intensity as calculated from ten simulations.

SRS amplifies fluctuations in the plasma, and so is sensitive to number of particles per cell used in the simulation, as can be seen in Figure 4.1. In this figure, the intensity

of SRS back-scattered light (denoted in this paper by $\langle I_{\text{SRS}} \rangle$) is plotted against the incoming laser intensity I_0 ranging between $0.4 - 4.0 \times 10^{15} \text{W/cm}^2$ for a homogeneous plasma with $n_e = 0.15n_{\text{cr}}$, $T_e = 4.5 \text{keV}$, for different numbers of particles per cell. At low incident intensity, $\langle I_{\text{SRS}} \rangle$ is inversely proportional to the number of PPC used. This is as we would expect for the case of simple convective amplification [Rosenbluth, 1972] of the product of two quantities (E_y, B_z) which vary as background PIC noise, which is proportional to $1/\sqrt{\text{PPC}}$. The upper saturated level of $\langle I_{\text{SRS}} \rangle$ is robust to the number of PPC for $\text{PPC} > 100$. The transition between these two levels represents the change from standard convective amplification of SRS to enhanced growth of SRS due to trapping (inflationary SRS), hence we call this the inflation threshold. The existence of an inflation threshold is also robust to the number of particles per cell for $\text{PPC} > 100$.

In the region containing the inflation threshold, the error associated with the intensity of SRS scattered light is largest. This suggests that inflationary SRS is very sensitive to the initial distribution of particles in the simulation domain, and that a statistical analysis of the mean and standard deviation of intensity across different random seeds will be important if we are to determine the iSRS threshold intensity accurately.

4.3 Diagnosing iSRS in inhomogeneous plasmas

Three signatures of inflationary SRS observed in the literature for homogeneous plasmas are: a threshold intensity past which scattering of laser light is enhanced above the level predicted by fluid theory [Vu et al., 2007]; electron-trapping in the SRS EPWs leading to local flattening of the distribution function at the EPW phase velocity [Vu et al., 2002]; and the growth of down-shifted SRS EPWs and a continuum of beam-acoustic modes (BAMs) [Yin et al., 2006]. In what follows we show that all of these signatures are also present for iSRS in an inhomogeneous plasma, despite the instability arising through an auto-resonance rather than a transition from convective to absolute growth.

4.3.1 Inflation threshold

We consider first the existence of a threshold intensity past which SRS growth is enhanced, by several orders of magnitude, above the predictions of fluid theory; this has been seen in experiments [Kline et al., 2006] and simulations [Riconda et al., 2011; Vu et al., 2002, 2007; Yin et al., 2006].

In order to identify kinetic inflation of the SRS scattered light intensity in our PIC simulations, we use the simple fluid model presented in Section 3.3.3 to calculate and compare the intensity of SRS scattered light in the absence of kinetic effects.

The red circular markers in Figure 4.2 show the results of applying this method to the case of a $500\mu\text{m}$ density scale-length plasma, with the density profile centred at $0.15n_{\text{cr}}$, for incident laser intensities ranging from $10^{14} - 10^{16} \text{W/cm}^2$. The blue triangular markers show the intensity of SRS scattered light calculated from the equivalent kinetic

EPOCH simulations. The relationship between the kinetic and fluid results changes as the incident laser intensity increases. At low intensities the fluid and kinetic models are well matched, but not identical, suggesting that there is always some kinetic element to the SRS behaviour in these simulations.

Continuing this analysis to intensities $< 10^{13} \text{W/cm}^2$ (well below those relevant to shock-ignition) shows that the two methods converge for low intensities, where the behaviour is purely fluid. Once the incident laser intensity exceeds $I_{\text{threshold}} \sim 1.4 \times 10^{15} \text{W/cm}^2$, the intensity of SRS scattered light measured in the kinetic simulations exceeds the fluid prediction by between one and three orders of magnitude, until the intensity reaches $I_0 = 10^{16} \text{W/cm}^2$, where it appears to saturate. In the fluid model, $\langle I_{\text{SRS}} \rangle$ is a smooth function of incident laser intensity and we cannot define such a threshold intensity. This implies that kinetic effects in our simulations are responsible for the increase in $\langle I_{\text{SRS}} \rangle$ and that we have observed iSRS. The fluid estimate shows no sign of saturating at high intensities, since the Rosenbluth gain formula used is based on unbounded linear SRS growth over the resonance region ℓ and the model does not include pump depletion.

By constructing plots such as these, which show the fully kinetic PIC results alongside results from our simple fluid model, we are able to identify the iSRS threshold as the point past which the kinetic and fluid models differ by at least one order of magnitude.

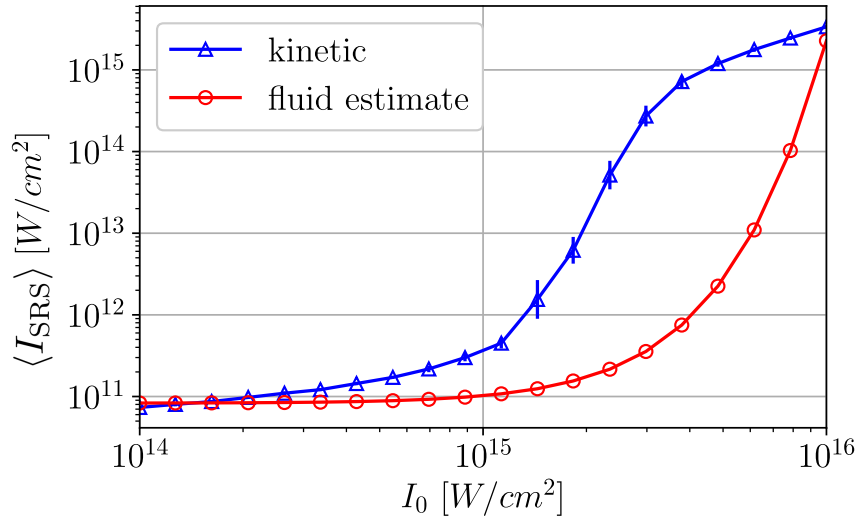


Figure 4.2: Blue triangular markers show the intensity of SRS scattered light calculated using the fully-kinetic EPOCH code for parameters: $L_n = 500 \mu\text{m}$ and $n_{\text{mid}} = 0.15 n_{\text{cr}}$. Red circular markers show the intensity of SRS scattered light calculated, for the same plasma parameters, from the fluid model presented above. The initial noise level in the fluid model was calculated from a PIC simulation without the laser driver: $I_{\text{noise}} = \langle E_y B_z \rangle_{x,t} / \mu_0 = 8 \times 10^{10} \text{W/cm}^2$.

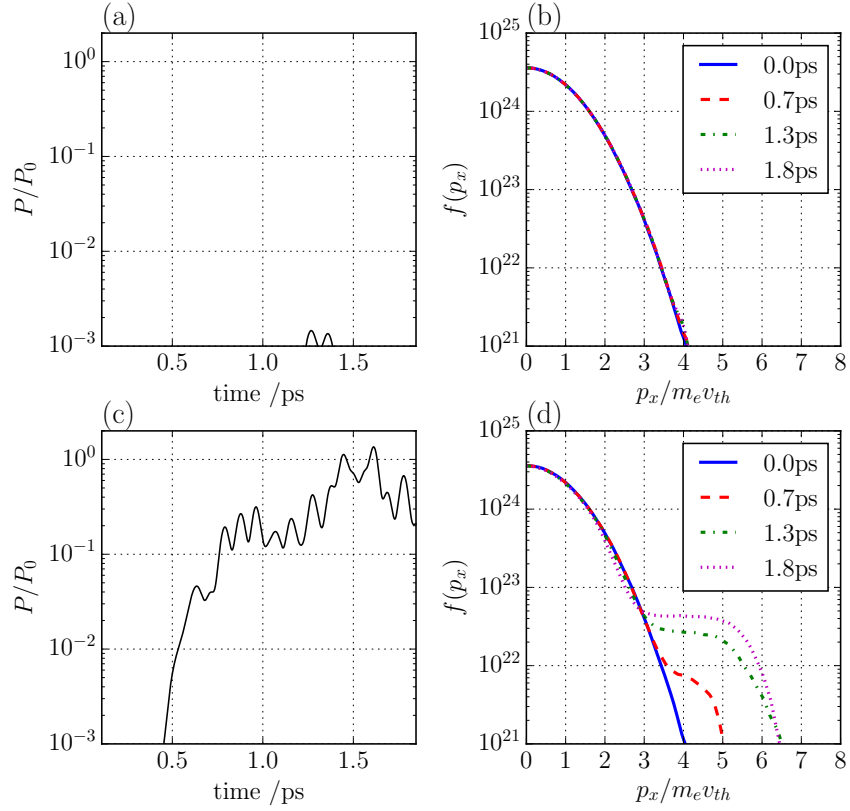


Figure 4.3: Time-resolved comparison of SRS-reflectivity (a,c) and electron distribution functions (b,d) for two simulations with parameters: $L_n = 500 \mu\text{m}$; centred at $0.15n_{\text{cr}}$; and $T_e = 4.5 \text{ keV}$. The distribution function of electron momentum is averaged over the entire spatial domain at four times, normalised to the initial thermal momentum. Panels (a,b) have an incident laser intensity below the threshold for inflationary SRS; $I_0 = 1.13 \times 10^{15} \text{ W/cm}^2$. Panels (c,d) have an incident laser intensity above the iSRS threshold; $I_0 = 4.83 \times 10^{15} \text{ W/cm}^2$.

4.3.2 Electron trapping

A second signature of iSRS, as reported in the literature for homogeneous plasmas, is electron-trapping in the SRS electron plasma waves, leading to a non-linear frequency shift and enhanced SRS-reflectivities at large $k\lambda_D$ [Vu et al., 2002]. A typical manifestation of this, for our inhomogeneous simulations, is shown in Figure 4.3. Figure 4.3 shows the instantaneous SRS-reflectivity measured at the left boundary of the simulation domain (a,c), alongside the box-averaged electron distribution function at four times (b,d), for two simulations with laser intensities above and below the iSRS threshold. Sub-figures 4.3 (a,b) show that, when driven below threshold, the distribution of electron momenta is Maxwellian throughout the simulation, and that the maximum instantaneous power in SRS-reflected light is consequently very low ($P \sim 10^{-3} P_0$). In sub-figures (c,d), where the incident laser intensity is well above the iSRS threshold, we see that the power in SRS-reflected light is correlated with the growth of a non-Maxwellian tail in the distribution function, corresponding to an electron population trapped in the SRS

electron plasma waves. There is a general trend of increasing SRS-reflected light that correlates with the increasing trapped electron population.

4.3.3 Nonlinear frequency shift

Electron-trapping in the SRS-driven EPW causes a time-dependent non-linear frequency shift of the EPWs [Kline et al., 2006; Morales and O’Neil, 1972], and the growth of a sequence of beam-acoustic modes [Yin et al., 2006]; this is the third signature of iSRS.

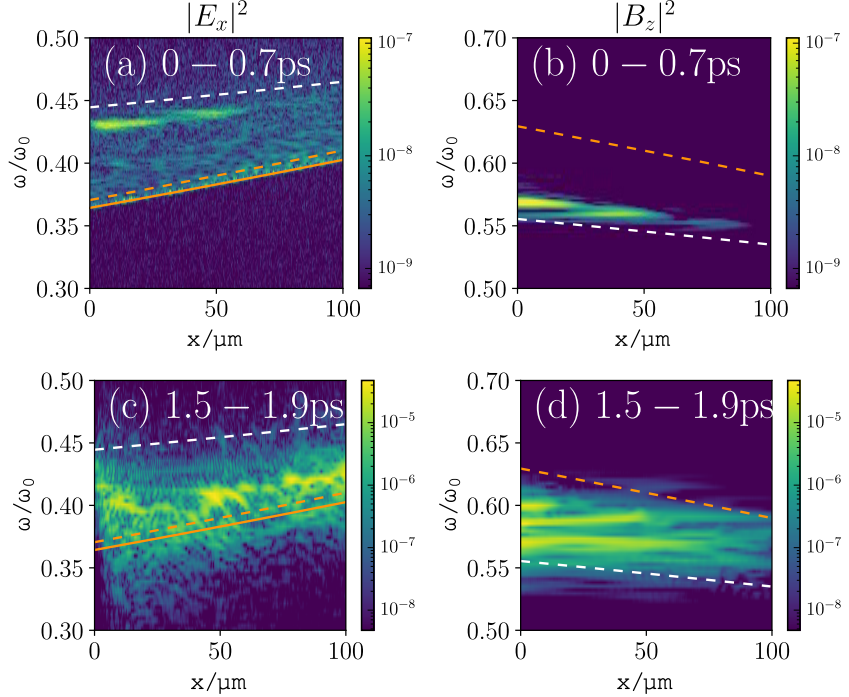


Figure 4.4: Top panels show the spectra of electrostatic (a) and electromagnetic (b) waves over the period 0 – 0.7ps. The white (orange) dashed lines represent the linear predictions for the spectra of backward (forward) SRS. The bottom panels show the same spectra calculated over the period 1.5 – 1.9ps. The E_x (B_z) spectrum is significantly down-shifted (up-shifted), demonstrating a trapped population of electrons in the EPW [Yin et al., 2006]. The orange solid line represents the plasma frequency ω_{pe} for the simulation parameters: $L_n = 500\mu\text{m}$ centred at $0.15n_{cr}$ and $I_0 = 4.83 \times 10^{15}\text{W/cm}^2$.

Figure 4.4 shows the spatially resolved frequency spectra of EPWs (a,c) and EMWs (b,d) at 0-0.7ps (a,b) and 1.5-1.9ps (c,d). In panels (a,b), the signal maxima sit very close to the white dashed line, which represents the frequencies predicted by the SRS matching-conditions for the original Maxwellian plasma. This means that, at early time, the SRS EPWs and their associated back-scattered light waves are excited at the frequencies matching those of the linear theory without trapping. They are slightly down-shifted from the analytical prediction, which suggests that the trapping becomes important almost immediately in our simulations. At later time, Figure 4.4 (c) shows that the EPW spectrum is down-shifted in frequency at every location in the simulation

domain, including to frequencies below the plasma frequency for the original Maxwellian plasma (orange solid line). This is evidence of a large trapped particle population removing energy from the wave, causing the frequency of the wave to decrease such that energy is conserved [Morales and O'Neil, 1972]. We also note that in Figure 4.4 (d) the back-scattered light spectrum is up-shifted in frequency space, so as to maintain frequency matching. As well as obvious up-shift of the electromagnetic spectrum, we can also see more general broadening as we move from Figure 4.4 (b) to (d). This could be caused by waves from a higher density propagating to smaller x , so that at a particular location the spectrum covers waves from a range of densities.

4.3.4 Beam acoustic modes

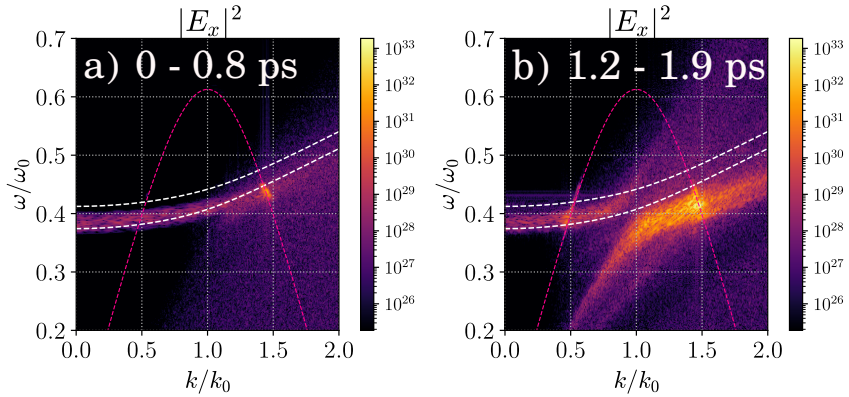


Figure 4.5: (a) 2D FFT of E_x over the period 0 – 0.8ps. (b) 2D FFT of E_x over the period 1.2 – 1.9ps. The white dashed lines represent the analytical dispersion relations corresponding to the minimum (bottom line) and maximum (top line) plasma densities, assuming a Maxwellian electron distribution. The pink dashed line shows the Stokes line for down-shifted EM waves. Simulation parameters: $L_n = 500\mu\text{m}$ centred at $0.15n_{\text{cr}}$ and $I_0 = 4.83 \times 10^{15}\text{W/cm}^2$.

Further evidence for a large trapped particle population can be seen in the growth of a beam acoustic mode in the electrostatic (ω, k) spectrum. Figure 4.5 shows the electrostatic dispersion relation from a simulation; it is calculated by taking a 2D Fourier transform of the E_x field over the entire spatial domain, and over two distinct time intervals. At early time, shown in Figure 4.5 (a), electron plasma waves are excited, from background noise, between the two white dashed curves. These represent the Bohm-Gross dispersion relations $\omega_{\text{EPW}}^2 = \omega_{\text{pe}}^2 + 3v_{\text{th}}^2 k_{\text{EPW}}^2$ for the highest density in the domain (top line) and the lowest density (bottom line). According to fluid theory, SRS will grow where the Stokes branch, defined by $(\omega - \omega_0)^2 = \omega_{\text{pe}}^2 + c^2(k - k_0)^2$, intersects with this dispersion curve. This fluid-SRS signal can be seen in Figure 4.5 (a).

The right hand panel of Figure 4.5 shows the EPW dispersion relation calculated from the simulation between 1.2 – 1.9ps. Inspection of the distribution function in Figure 4.3 shows that, at these times, the distribution function is modified from the

initial Maxwellian and has a large flattened region, which acts as an effective beam population [Yin et al., 2006]. According to linear theory, this change in the distribution function f changes the kinetic dispersion relation for the electrostatic waves in the system, defined by: $\epsilon(\omega, k) = 1 - \frac{q_e^2}{\epsilon_0 m_e k} \int \frac{\partial f / \partial v}{v - \omega/k} dv = 0$. This change in the dielectric properties of the plasma is realised in the (ω, k) spectrum as a continuum of beam acoustic modes [Yin et al., 2006], this is the large spectral feature in the right hand panel of Figure 4.5 that sits strictly below the Bohm-Gross dispersion curves. These beam acoustic modes are frequency downshifted, recovering the result from Morales and O’Neil’s non-linear analysis[Morales and O’Neil, 1972]. The maximum of the BAM signal at $k \sim 1.5k_0$ is the intersection of the BAM with the Stokes branch, the new location of SRS growth.

We can also see in Figure 4.5 (b) a signal at $k \sim 0.5k_0$ which sits on the intersection of the Stokes branch with the range of EPWs satisfying the Bohm-Gross dispersion relations. This represents forward-scattered SRS EPWs, which have not undergone a significant frequency shift. For all the simulations presented in this paper, when driven above threshold, the power in forward SRS scattered light is of the order $P \sim 10^{-3}P_0$ or lower, and is therefore energetically unimportant.

4.4 Intensity threshold and hot electron scaling

Using the method developed in Section 4.3 for locating the inflation threshold, and the analysis of electron trapping and downshifted EPWs to ensure that the SRS observed is inflationary in origin, we investigate how iSRS depends on various plasma parameters relevant to shock-ignition. Using the PIC simulation set-up as in Section 4.2 (with the same simulation domains, plasma densities, and temperatures), we varied the plasma density scale-length across the range of values predicted for shock-ignition ($300\mu\text{m} - 1000\mu\text{m}$) [Ribeyre et al., 2009]. As well as varying the density scale-length, we also centred the density profiles at different values of density. Figure 4.6 shows the result of this parameter scan.

From Figure 4.6 (a) we see that as the density scale-length of the SI coronal plasma decreases, the intensity threshold for iSRS increases. Vu et al. (2007) [Vu et al., 2007] derived a condition for the kinetic inflation threshold of SRS in a homogeneous plasma. They showed that the magnitude of the trapped electron potential energy in the EPW must be greater than or equal to the energy gained by a particle in one complete trapped orbit due to velocity diffusion in the background plasma fluctuations. This ensures that trapping remains for at least one bounce period.

No such analytic threshold has been derived for an inhomogeneous plasma. However, when L_n is smaller the inhomogenous gain is smaller and the amplitude reached by convective amplification of the SRS EPW is lower for the same intensity. Hence SRS in a shorter density scale length plasma is less likely to generate EPWs with sufficient amplitude for electron trapping effects to trigger the transition to iSRS.

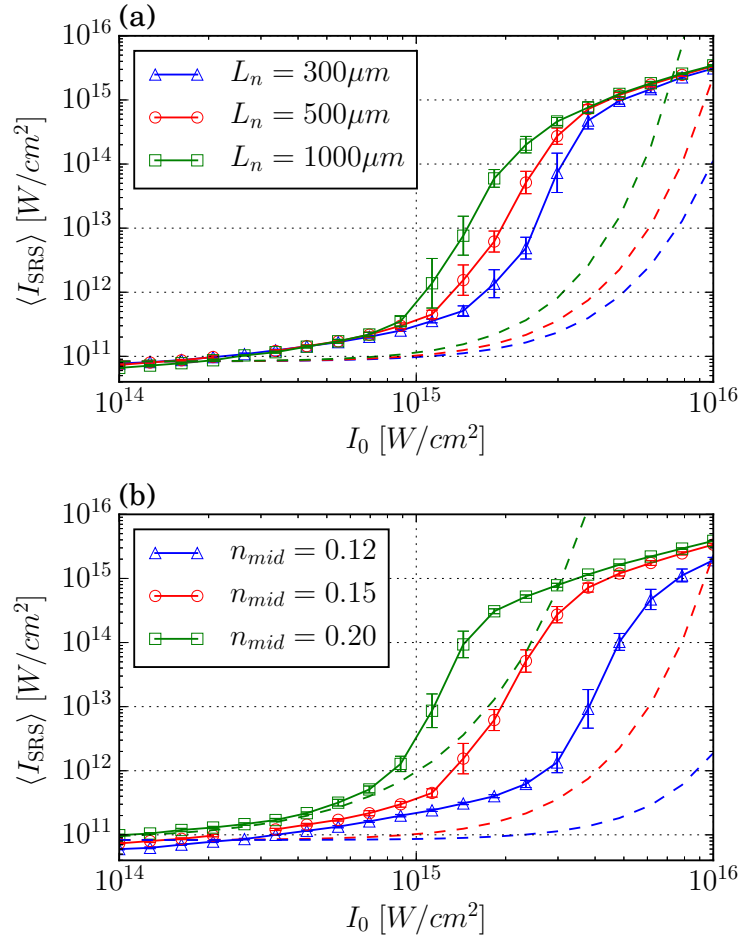


Figure 4.6: (a) Relationship between incident laser intensity and the intensity of SRS scattered light for three different density scale-lengths, with plasma density profiles centred at $0.15n_{cr}$. (b) Relationship between incident laser intensity and the intensity of SRS scattered light for three simulations with $L_n = 500\mu\text{m}$ centred at three different densities. Each coloured dashed line represents the prediction of the fluid model presented in Section 4.3 for the same parameters as the solid line of the same colour.

Figure 4.6 (b) shows the measured intensity of SRS scattered light in three sets of simulations with density profiles centred at $0.12, 0.15, 0.20n_{cr}$, chosen so that the density ranges do not overlap (see Table 4.1). As the central density decreases, the intensity threshold for iSRS increases. As for the case of varying scale-lengths changing the threshold, this can be explained in terms of the Rosenbluth gain [Rosenbluth, 1972]. For a fixed density scale-length, as the density decreases, the Rosenbluth gain exponent also decreases. This means that the fluid gain through convective SRS is reduced. Hence SRS at a low density is less likely than that at higher density to generate EPWs with sufficient amplitude for electron trapping effects to trigger the transition to iSRS. For the parameters of Figure 4.7 (b) with $I_0 = 6.16 \times 10^{15}\text{W/cm}^2$, the Rosenbluth gain exponent increases from ~ 1 to ~ 25 as the densities increase.

As well as understanding how the density scale-length of the plasma and the density

at which iSRS is driven affects the iSRS threshold, we would like to understand how these factors affect the hot electron population. We consider three simulations from Figure 4.6 (a) with $I_0 = 2.98 \times 10^{15} \text{ W/cm}^2$, and three from Figure 4.6 (b), with $I_0 = 6.16 \times 10^{15} \text{ W/cm}^2$. Figures 4.7 (a,b) show the hot electron population in these simulations, in the form of histograms for the electron flux through the right boundary.

Figure 4.7 (a) shows the electron distribution function resulting from iSRS for three density scale-lengths. These are for a laser intensity above the onset threshold for iSRS but below an intensity which would lead to saturation. All results are for the same central density. The most prominent difference is that the peak electron energy increases with decreasing density scale-length. This results from the fact that the shorter density scale-length simulation access a higher peak density since the simulation domain size is the same for all three cases. The SRS matching conditions for these higher densities result in a higher phase speed of driven EPWs. Solving the SRS matching conditions for these densities, we find that the hot-electron energies calculated from the phase velocities are between 35 – 50keV for all three cases.

Figure 4.7 (b), however, shows a clear dependence of the hot electrons from iSRS on density. As the density increases the maximum hot- electron kinetic energy also increases in line with the increase in SRS EPW phase velocities. Over the 2ps of the simulations the fraction of incident laser energy converted into hot-electrons with energy $> 100\text{keV}$ are: 0, 0.002, and 0.15 for the $0.12, 0.15, 0.20n_{\text{cr}}$ densities. For the density scale-lengths $L_n = 300, 500, 1000\mu\text{m}$ the fractions of incident laser energy converted into $> 100\text{keV}$ hot- electrons are: 0.005, 0.001 and 0 respectively.

4.5 Saturation

Several saturation mechanisms for iSRS in PIC simulations have been proposed, depending on the physical mechanisms present in the simulation. For simulations in 1D with immobile ions, there are three possible saturation mechanisms for SRS undergoing autoresonance: wave-breaking of the plasma wave; pump depletion of the laser driver; and frequency shift such that the autoresonance condition is no longer satisfied. In simulations with mobile ions and in higher dimensions, additional saturation mechanisms have been identified for iSRS in a homogeneous plasma. These additional saturation mechanisms are: Langmuir decay instability (LDI); wavefront bowing of the EPW; the trapped particle modulation instability (TPMI); and self-focusing [Yin et al., 2007].

We can eliminate EPW wave-breaking as the saturation mechanisms in our simulations as the maximum normalised EPW energy well below the wave-breaking limit in all cases. Take, for example, the simulation corresponding to $I_0 = 7.83 \times 10^{15} \text{ W/cm}^2$ on the red curve of Figure 4.6 (a). We can calculate the wave-breaking limit across the density range to be $E_{\text{WBe}}/m_e c \omega_0 = 0.024 - 3.52$; but the maximum EPW energy in the simulation is $E_{\text{EPWe}}/m_e c \omega_0 = 0.0056$, well below the limit. Figure 4.8 shows the Poynting flux of the scattered light (a) and incident laser (b) for a simulation

with intensity in the saturated regime ($I_0 = 7.83 \times 10^{15} \text{W/cm}^2$). We can see complete depletion of the pump correlated with the maximum intensity of scattered light first at approximately $x = 45\mu\text{m}$, $t = 0.8\text{ps}$. It is interesting to note that iSRS at low densities is depleting the pump before it can reach higher densities, where the growth of SRS would be even greater.

Finally, we consider saturation due to the non-linear frequency shift which destabilises the auto-resonance.

4.6 Conclusion

Inflationary SRS has been detected in PIC simulations of a inhomogeneous plasmas with parameters relevant to the shock-ignition model of ICF. This study demonstrates an iSRS threshold $I_{\text{threshold}} \lesssim 5 \times 10^{15} \text{W/cm}^2$ across the whole range of parameters tested and that the location of this threshold depends on the density scale-length L_n . For the case with $L_n = 500\mu\text{m}$ and $I_0 = 4.83 \times 10^{15} \text{W/cm}^2$ significant iSRS would occur at $0.15n_{\text{cr}}$ generating hot-electrons with mostly $< 100\text{keV}$ energies and depleting the laser drive available at higher densities. This is potentially beneficial to shock-ignition in that these electrons are likely to enhance the ignitor shock and prevent significant SRS at higher densities, potentially absolute at $0.25n_{\text{cr}}$. SRS at higher densities is likely to generate electron distributions with a higher percentage of $> 100\text{keV}$ electrons than that from iSRS at lower densities. These results suggest that a potential route to use iSRS to the advantage of shock-ignition, assuming all SRS cannot be removed by other means, would be for the shock ignitor pulse to have the largest possible amplitude. This would ensure significant iSRS at lower densities and generate only hot-electrons with energies below 100keV. This in turn would pump deplete the laser reducing SRS at higher densities which could generate hot-electrons with energy above 100keV. These conclusions are however only valid for the restricted 1D, collisionless simulations presented in this paper and more detailed simulations, as outlined below, would be needed to fully assess the hot-electron distribution and its impact on SI schemes.

The simulations presented in this paper highlight the importance of a thorough investigation of iSRS for any shock-ignition plans. These results are however a first study of the plasmas parameters where iSRS may occur. A full theoretical investigation of the potential impact of iSRS on shock-ignition will require significantly larger scale simulations. Of particular importance are multi-dimensional effects and laser speckle profiles. These would allow the competition between SRS and TPD as sources of hot-electrons to be assessed in two and three dimensions. The transverse non-uniformity associated with multi-dimensional effects is likely to affect iSRS through trapped electron side losses and a broader spectrum of EPWs resulting from side-scatter and TPD. Furthermore, the auto-resonance responsible for iSRS in these simulations may not be possible when a full speckle profile is included; since the extension of the resonance region may take the resonant waves outside of an individual speckle. The use of broadband

laser systems to mitigate LPI will also need to be assessed in the kinetic regime of iSRS. All of these refinements to iSRS simulations will require considerably more computing resources but are none-the-less needed for a comprehensive treatment of LPI relevant to shock-ignition.

Talk more and cite about how things change as you move to higher dimensions

This work is nowhere near finished in fact it's a bit crap

Write a bit about Christoferetti's reviewers comments and how their must be some effect caused by the damping as well as autoresonance.

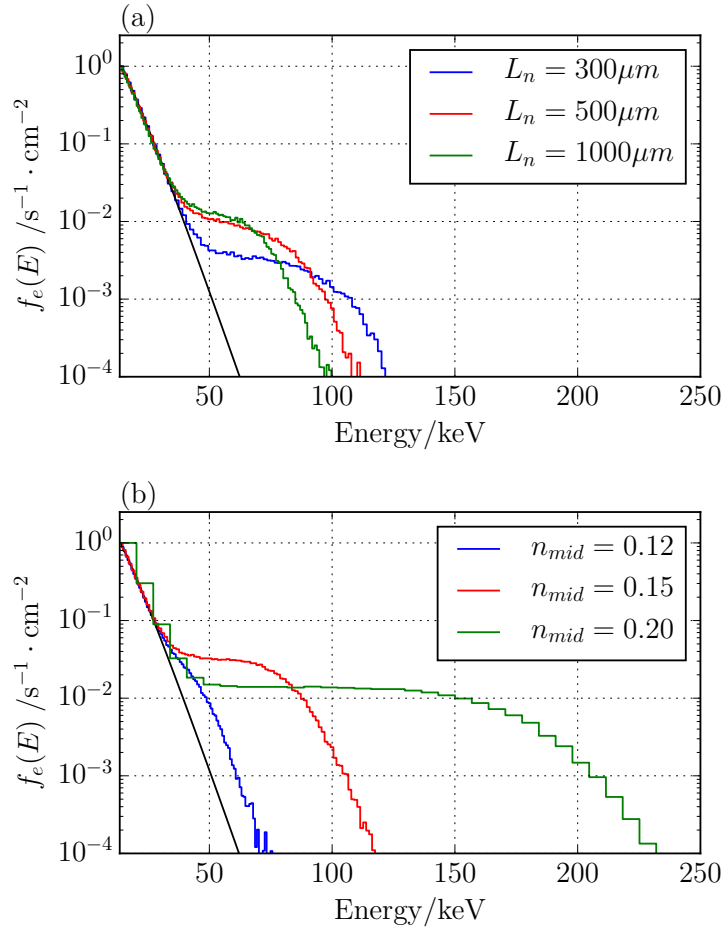


Figure 4.7: (a) Hot electron flux through the right boundary in three simulations with parameters: $I_0 = 2.98 \times 10^{15} \text{W/cm}^2$; $n_{\text{mid}} = 0.15n_{\text{cr}}$; $L_n = 300, 500, 1000 \mu\text{m}$. (b) Hot electron flux through the right boundary in three simulations with parameters: $I_0 = 6.16 \times 10^{15} \text{W/cm}^2$; $L_n = 500 \mu\text{m}$; $n_{\text{mid}} = 0.12, 0.15, 0.20n_{\text{cr}}$ respectively. Each distribution is normalised to its maximum value. The smooth black line corresponds to the equivalent flux for a Maxwellian distribution with $T_e = 4.5 \text{keV}$, for comparison with the bulk plasma.

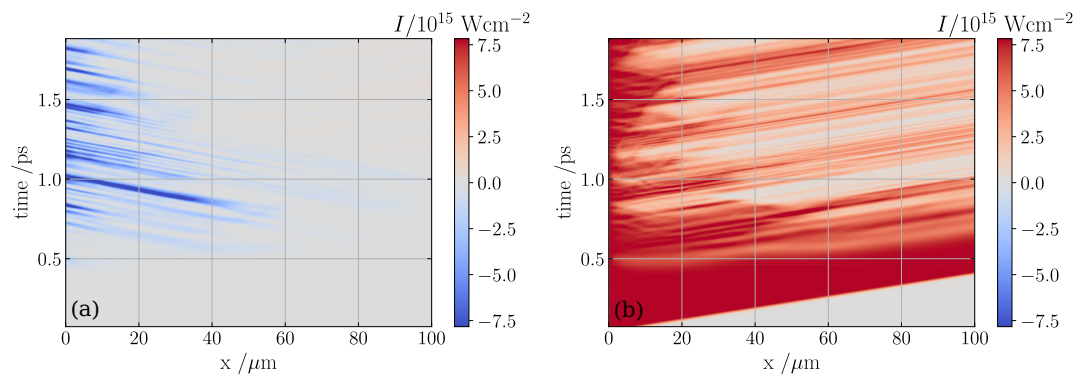


Figure 4.8: (a) Poynting flux of scattered light (b) laser energy, showing significant depletion of the pump. Simulation parameters: $L_n = 500\mu\text{m}$ centred at $0.15n_{\text{cr}}$ and $I_0 = 7.83 \times 10^{15}\text{W/cm}^2$.

Chapter 5

Effects of laser bandwidth on inflationary stimulated Raman scattering

In this chapter, results of one-dimensional PIC simulations are presented, which represent the first investigation into the practical possibility of using broadband to suppress inflationary SRS in shock-ignition. The chapter begins with a review of the literature discussing suppression of SRS by broadband lasers. We then show that for a decoupled broadband laser, the non-linear frequency shift must be taken into account when calculating the condition for suppression of iSRS. Next we consider the case of realistic shock-ignition schemes on three laser systems: frequency-tripled Nd : glass; Krypton Fluoride (KrF); and Argon Fluoride (ArF). In each of these cases we model the predicted maximum realistic bandwidth in its physically-correct functional form. The chapter concludes with a discussion of the limitations of the modelling done so far, and suggestions for future work.

N.B. In this chapter, bandwidths are given in units of tera-Hertz (THz) since this is standard in the literature. This can be converted to radians per second through the relation $\Delta\omega = 2\pi\Delta f$.

5.1 Motivation and literature review

Early results in the 1970s suggested that finite-bandwidth laser drivers could change the behaviour of parametric instabilities. These studies considered a variety of parametric instabilities, including: the parametric decay instability [Thomson and Karush, 1974]; stimulated Brillouin scattering [Kruer et al., 1973]; and stimulated Raman scattering [Raymer et al., 1979]. Recently, broadband suppression of parametric instabilities has, once again, become a fashionable topic of discussion. All lasers have some natural bandwidth, which arises from quantum effects. However, for the majority of lasers relevant to ICF, this natural bandwidth is far too small to affect parametric instabilities.

There are various ways that additional bandwidth can be introduced into a laser system, including: induced spatial incoherence (ISI) [Lehmberg and Obenschain, 1983]; smoothing by spectral dispersion (SSD) [Skupsky et al., 1989]; stimulated rotational Raman scattering (SRRS).

As discussed in Chapter 4, Stimulated Raman Scattering (SRS) is a parametric instability of major concern to shock ignition; since it scatters light away from the target, and drives electron plasma waves to large amplitudes which then damp and send hot electrons towards the cold fuel. As such, many people are interested in the possibility of using broadband laser systems to suppress the growth of SRS in shock-ignition coronal plasmas. In the following literature review, we consider each of the main forms of SRS separately: absolute; convective-fluid; inflationary; and multi-beam. The original work presented in this chapter focuses on inflationary SRS, but we believe that it must be placed in its proper context by reviewing the literature for all types of SRS, since these are often concurrent and may all be present in the shock-ignition plasma corona.

5.1.1 Absolute SRS

[Thomson and Karush \[1974\]](#) showed that for an absolute parametric instability, with homogeneous growth rate γ_0 driven by a laser with bandwidth $\Delta\omega$, if $\Delta\omega > \gamma_0$ then the growth rate of the instability is reduced by a factor of $\gamma_0/\Delta\omega$.

PIC modelling of absolute SRS at low density and temperature ($n_e = 0.08n_{cr}$, $T_e = 100\text{eV}$, corresponding to $k_{EPW}\lambda_D \sim 0.08$) performed by [Zhao et al. \[2015\]](#) demonstrates the suppression of the SRS growth rate by frequency-modulated SSD-type bandwidth. They find that the suppression effect is increased by increasing the bandwidth; and that for a fixed bandwidth, the suppression depends on the modulation frequency. They also note that the bandwidth has no effect on the saturated level of SRS, only the growth rate. In their conclusion they stress the importance of considering the temporal structure of the laser field in each bandwidth investigation. In a follow-up paper [Zhao et al. \[2017b\]](#) consider SRS driven by incoherent light which is composed of a large number of beamlets each with different frequency and phase (called a decoupled broadband laser (DBL)). For very large bandwidths (on the order of $10\%\omega_0$) they find that the growth rate of backward SRS is reduced compared to the frequency-modulated light with the same bandwidth, but that the scattered light still saturates at the same level as with no bandwidth.

The work of [Zhou et al. \[2018\]](#) develops the theory of absolute-SRS suppression by DBL-type bandwidth by considering the “highly nonlinear”, kinetic case where $k_{EPW}\lambda_D = 0.3$. As well as confirming the suppression of the growth rate measured in [[Zhao et al., 2015, 2017b](#)], they find that bandwidth in the range 2.25% to 3.0% actually acts to *enhance* SRS in the so-called “deep nonlinear stage” by increasing the resonant range in line with the non-linear frequency shift. The authors conclude that a broadband laser light is not an appropriate choice for suppression of absolute SRS on a

several picosecond time-scale.

5.1.2 Fluid convective SRS

We have seen, in the previous section, that absolute SRS can be suppressed using random bandwidth [Thomson and Karush, 1974]; deterministic frequency-modulated bandwidth [Zhao et al., 2015]; and bandwidth from a DBL [Zhao et al., 2017b; Zhou et al., 2018]. This is not true, however, for convective SRS in an inhomogeneous plasma. It was shown by Guzdar et al. [1991] that bandwidth in the form of random phase modulation reduces the growth rate of SRS, but it also increases the length of the resonance region. For a system with the laser and plasma satisfying certain conditions, these two effects cancel out and the bandwidth has no net effect on the SRS gain. The conditions for exact cancellation are: the homogeneous growth rate and bandwidth are much smaller than the plasma frequency at the resonance point ($\gamma_0, \Delta\omega \ll \omega_{pe}(x_{res})$); the length of the interaction region and coherence length are less than the plasma size ($\ell, c/\Delta\omega < L_x$); and that the homogeneous growth rate is much smaller than the bandwidth ($\gamma_0 \ll \Delta\omega$) Guzdar et al. [1991]. This analytical result tells us that random phase modulation will not be sufficient to suppress convective SRS.

It may be possible, however, to suppress convective SRS by using a decoupled broad-band laser (DBL). Zhao et al. [2017b] apply their theory of absolute SRS suppression in a homogeneous plasma by DBLs, to the case of convective SRS in an inhomogeneous plasma. For a plasma with a linear density profile and constant temperature such that $k_{EPW}\lambda_D \ll 0.25$ throughout, they compare the electrostatic energy present in the simulation in the cases $\Delta\omega_0 = 0, \Delta\omega_0 = 15\%$. They find that for the 15% bandwidth case, the electrostatic energy is reduced compared to with zero bandwidth and conclude that the linear convective SRS has been suppressed [Zhao et al., 2017b]. In a second paper the same year, Zhao et al. [2017a] consider the case of an inhomogeneous plasma density profile relevant to indirect-drive ICF.

An analytic description of this effect is given in Zhao et al. [2019]; they find that SRS can be well-controlled for a laser beam structure of multiple frequency components and total bandwidth of a few percent. By considering the frequency difference between any two beamlets, they find that there is a critical frequency difference below which the SRS instability regions for the beamlets overlap to form a single instability region. In this case, the two beamlets can be coupled with one EPW, leading to a higher growth rate for SRS. This effect is demonstrated in 1D PIC simulations, which show that SRS can grow to a high level if the beamlets satisfy this coupling condition, even if the total bandwidth is very large.

They derive a gain exponent for standard convective SRS driven by two beamlets of different frequencies, and find that two beamlets are independent when

$$\delta\omega_0 \geq \frac{\pi n_0 c (\omega_0^2 - \omega_{pe}^2)^{3/2}}{8 L \omega_0 \omega_L^2 \nu_p^2}. \quad (5.1)$$

Importantly, this condition is independent of the amplitude of the incident laser. In theory, this condition would allow us to construct a DBL to suppress SRS in a large-scale inhomogeneous plasma, however, secondary amplification of back-scattered light by one of the beamlets is a possibility. We must therefore consider another threshold for this secondary amplification: $\delta\omega_0 > \omega_{L1} - \omega_{L2}$ where $[\omega_{L1}, \omega_{L2}]$ is the range of EPW frequencies excited by SRS in the plasma (not including nonlinear frequency shift).

The parameters considered in this study are $\lambda_0 = 0.33\mu\text{m}$, $T_e = 2\text{keV}$, $n_e = [0.08, 0.12]n_c$, giving $k_{\text{EPW}}\lambda_D \sim [0.26, 0.35]$, well within the kinetic regime for SRS.

5.1.3 Inflationary SRS

[Wen et al. \[2021\]](#) derive a condition for the maximum gain of SRS driven by a sinusoidally frequency-modulated broadband laser, when the velocity of the resonance point is equal to the group velocity of the back-scattered light for as long as possible. By tuning the plasma parameters and/or laser parameters away from this condition, they can increase the threshold for kinetic SRS [\[Wen et al., 2021\]](#). The maximum gain criteria is given by the expression:

$$\Delta\omega\omega_m = \omega_{pe}c/2L_n, \quad (5.2)$$

and is verified through PIC simulations in the kinetic and fluid regimes. The left-hand side of Eq. 5.2 represents the maximum chirp ($|\partial_t\omega_0(x, t)|$) of the laser, and the right-hand side gives an expression for the spatial detuning due to density inhomogeneity. Several simplifying assumptions are made by the authors which allow them to derive this expression for the spatial detuning. Most importantly for our work, they omit the contribution of the non-linear frequency shift in their calculation of the velocity of the resonance point.

A key result of this work is that the threshold for iSRS driven by a sinusoidally frequency-modulated laser is independent of the bandwidth or frequency modulation alone, rather it depends on their product. Figure 5.1 shows results from our benchmarking of Wen's work. In this benchmarking study we recovered the results of their Osiris study using our own PIC code, EPOCH. We ran several simulations with fixed maximum normalised chirp ($\Delta\omega\omega_m/\omega_0 = 5.5 \times 10^{-6}$) and varied bandwidth. We find that the inflation threshold has a weak dependence on the bandwidth alone. From this preliminary investigation, we were confident in our laser set-up and in the use of EPOCH for this project.

Estimate size of this contribution in my cases and hope it is ignorable

5.1.4 Multi-beam SRS

Studies have also been performed using the code LPSE which show that, at ignition scales, absolute multi-beam backward SRS can be mitigated with bandwidth $\sim 1.6\%$ [\[Follett et al., 2021\]](#).

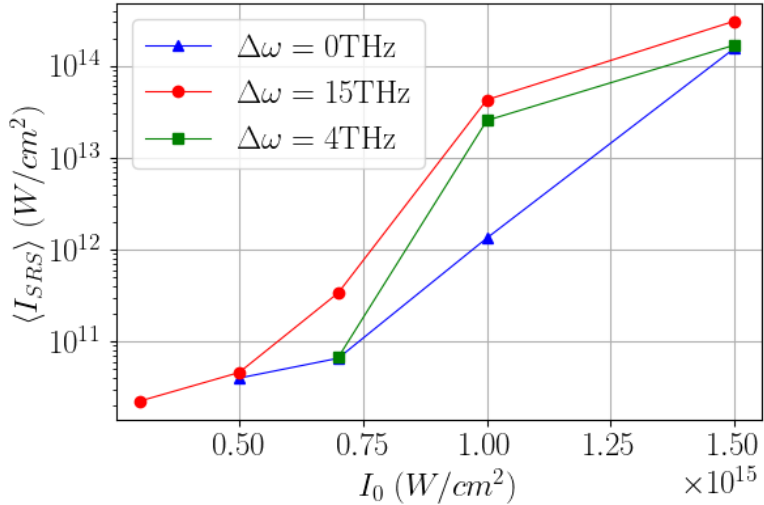


Figure 5.1: Intensity of light scattered by SRS, averaged over the last three picoseconds of each simulation, for three laser set-ups with fixed maximum normalised chirp ($\Delta\omega\omega_m/\omega_0 = 5.5 \times 10^{-6}$) and varied bandwidth. The simulation parameters common to all data-points are: $T_e = 4\text{keV}$; $L_n = 400\mu\text{m}$; $n_e(x) = 0.11n_{\text{cr}}\exp(x/L_n)$; PPC=16,000.

5.2 Decoupled broadband lasers

The work in this section was presented at the 62nd annual meeting of the American Physical Society Division of Plasma Physics in November 2020.

To begin our investigation of the effect of broadband on inflationary SRS, we focussed on the most relevant papers in the literature at the time ([[Zhao et al., 2019](#)]). This body of work concerns convective SRS in an inhomogeneous plasma, driven by a decoupled broadband laser.

A decoupled broadband laser is defined in Ref [Zhao et al. \[2017b\]](#) as

$$a_{\text{DBL}} = \sum_{i=1}^N a_i \cos(\omega_i t + \phi_i), \quad (5.3)$$

where a_i, ω_i, ϕ_i are the amplitude, carrier frequency, and phase of each of the N beamlets. The central frequency and wavelength of the laser is (ω_0, k_0) and the total frequency spectrum bandwidth is $\Delta\omega_0$.

In [Zhao et al. \[2019\]](#) they consider the suppression of parametric instabilities in a homogeneous plasma by decoupled broadband lasers (DBL).

5.2.1 Conclusions

In conclusion, we decided not to pursue out investigation of DBL-type bandwidth any futher since a) there are no plans to impliment it on lasers of interest and b)

5.3 Realistic laser bandwidth

This section concerns the results of our investigation into broadband suppression of inflationary SRS on different broadband laser systems. The particular form of the broadband may not seem like an important factor to us, but to the EPWs it can be very important. We consider shock-ignition driven by three different laser systems: frequency-tripled Nd : glass lasers, such as the NIF and LMJ; KrF lasers; and ArF lasers. Each laser has a different frequency and native bandwidth.

NRL provided us with density, temperatyre and intensity lineouts in 1D from simulations of shock-ignition on these three laser systems. We selected a single time slice, just before the interaction pulse enters the under-dense plasma created by the assembly pulse. Their simulations were performed using the rad-hydro code

For all the simulations presented in this section, the following EPOCH parameters are constant: $\Delta x = \min_x(\lambda_D)$; PPC = 2000; $T_{\text{end}} = 6\text{ps}$; thermal boundaries for particles; field boundaries are laser (x_{min}), and absorbing boundaries (x_{max}). We treat the ions as a neutralising background population to allow us to pinpoint the effect of bandwidth on inflationary SRS only. The incident laser intensity is set to be approximately the threshold intensity for inflationary SRS. The threshold intensity is found by varying the intensity for identical PIC set-ups to find the minimum intensity such that the time-averaged intensity of scatter from bSRS is greater than 10% of the incident laser intensity.

Wavelength / nm	Frequency / THz	Intensity / 10^{15}Wcm^{-2}	Bandwidth / THz	Bandwidth / % ω_0
351	854	0.4 to 4.0	0, 1, 10	0, 0.12, 1.2
248	1209		0, 3, 6	0, 0.25, 0.50
193	1553	4×10^{15}	0, 5, 8, 10	0, 0.32, 0.52, 0.64

Email
and ask
what
code
they
used

Table 5.1: Laser parameters for this investigation. Where multiple values are presented in a list, each represents a different simulation. The incident laser intensity is set to be approximately the threshold intensity for inflationary SRS. The choice of bandwidths and their implementations in EPOCH are explained and referenced in Sections 5.4, 5.5, 5.6, for the 351, 248, 193 nm cases respectively.

Wavelength / nm	L_x / μm	T_e / keV	n_e / n_{cr}	ω_{pe} / ω_0	L_n / μm
351	270	5.4	[0.105, 0.175]	[0.33, 0.42]	[420, 590]
248	270	3.4	[0.078, 0.137]	[0.27, 0.38]	[400, 550]
193	275	3.5	[0.071, 0.140]	[0.26, 0.37]	[330, 470]

Table 5.2: Table shows plasma parameters from simulations performed at the NRL, chosen such that $k_{\text{EPW}}\lambda_D$ is between 0.3 and 0.45. The temperature given is the maximum temperature of the particles initialised at $t = 0$, as there is, in reality, a slight temperature gradient in the electron profile.

5.4 351nm Nd : glass laser

5.4.1 Base case: $\Delta f = 0$

As stated in Section 5.3, the plasma density and temperature profiles are taken from the library of radiation hydrodynamic simulations at the Naval Research Laboratory.

Sorry this is a horrible way to write this, but this is the detailed plasma set-up: $T_e(x) = \sum_{i=0}^3 T_i x^i$, $n_e(x) = n_{\text{cr}} \sum_{i=0}^3 n_i x^i$; $\{T\}_i = \{3.01, 1.47 \times 10^3, 1.31 \times 10^6, -2.27 \times 10^9\}$; $\{n\}_i = \{0.07, 165, 3.95 \times 10^4, 1.01 \times 10^9\}$.

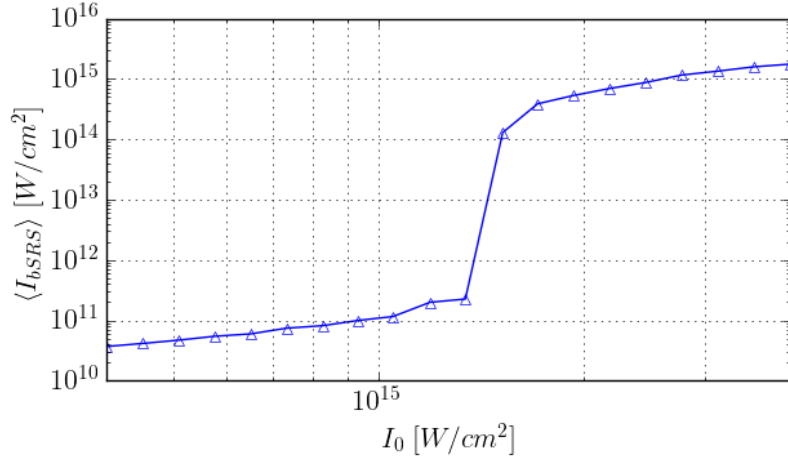


Figure 5.2: Intensity of light scattered by backward SRS, time-averaged for all $t > 2\text{ps}$. The incident laser intensity varies between $4 \times 10^{14}\text{W}/\text{cm}^2$ and $4 \times 10^{15}\text{W}/\text{cm}^2$.

5.4.2 SSD-type bandwidth: $\Delta f = 1\text{THz}$

1THz is the maximum bandwidth currently implemented by SSD on a 351nm laser, achieved at the Omega laser facility [Regan et al., 2005]. According to Wen et al. [2021], in order to increase the iSRS threshold we require that the modulation frequency satisfies $\omega_m \gg \omega_{pe}c/2L_n\Delta\omega$. From the plasma parameters given in Table 5.2 and bandwidth of 1THz, this requirement becomes: $\omega_m \gg 128\text{THz}$. This is problematic, since the optimal modulation frequency for SSD-type smoothing is on the order of 10GHz = 0.001THz [Kelly et al., 2013; Regan et al., 2005].

We can implement a continuous-bandwidth frequency-modulated laser in EPOCH using the standard EPOCH laser-driver like so:

$$\begin{aligned} E(x, t) &= E_0 \sin(\omega_0 t - \phi(x, t)) \\ \phi(x, t) &= \frac{1}{2} \frac{\Delta\omega}{\omega_m} \sin\left(\omega_m t - \frac{\omega_m}{c}x\right). \end{aligned} \tag{5.4}$$

5.4.3 Optical parametric amplification: $\Delta f = 10\text{THz}$

According to [Lehmberg et al. \[2020\]](#) “Parametric amplification may allow bandwidths up to 10 THz from 351 nm glass systems...”.

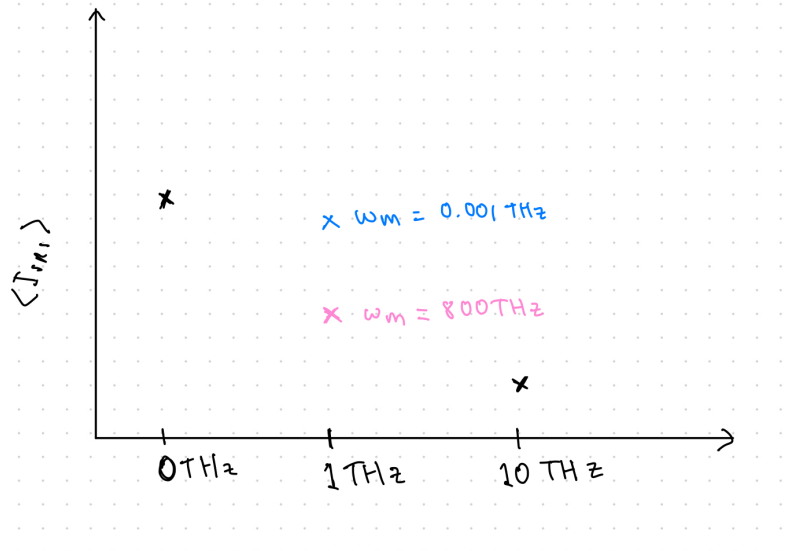


Figure 5.3: placeholder figure for Nd glass sim results

5.5 248nm krypton fluoride

5.5.1 Base case: $\Delta f = 0$

5.5.2 Intrinsic bandwidth: $\Delta f = 1, 2, 3$ THz

Intrinsic bandwidth of KrF laser such as Nike is predicted to be 3Thz [[Obenschain et al., 2015](#)]

5.5.3 Self phase modulation: $\Delta f = 4, 5, 6$ THz

According to this paper: ”Stimulated rotational Raman scattering of arbitrarily polarized broadband light” [[Lehmberg et al., 2020](#)] the SPM bandwidth of KrF limited to 6THz cos of physics.

5.6 193nm argon fluoride

Excimer lasers have a broad amplification spectrum in the UV when compared to Nd: glass lasers. In this section we consider the argon fluoride (ArF) laser under development at the NRL, which is predicted to have native bandwidth up to 10THz [[Obenschain et al., 2020](#)].

5.6.1 Base case: $\Delta f = 0$

Sorry this is a horrible way to write this, but this is the detailed plasma set-up: $T_e(x) = \sum_{i=0}^3 T_i x^i$, $n_e(x) = n_{\text{cr}} \sum_{i=0}^3 n_i x^i$; $\{T\}_i = \{3.01, 1.47 \times 10^3, 1.31 \times 10^6, -2.27 \times 10^9\}$; $\{n\}_i = \{0.07, 165, 3.95 \times 10^4, 1.01 \times 10^9\}$.

5.6.2 Intrinsic bandwidth: $\Delta f = 5, 8, 10$ THz

In this section, we perform a series of simulations at different bandwidths which are considered realistic for ArF laser systems currently under development [Obenschain et al., 2020]. To model the continuous laser spectrum, we follow the method presented in Bates et al. [2020] and distribute 50 beamlets of different frequencies around the central frequency. The intensities of the lines follow a Gaussian distribution whose FWHM is given by the laser bandwidth. Follett et al. [2019] says 50 is enough for a gaussian beam up to 10 percent. Each beamlet has a random phase so the total driven laser field looks like this:

$$E(x, t) = \sum_{i=1}^{50} E_i \sin(\omega_i t + \phi_i) \quad (5.5)$$

$\phi_i \in [0, 2\pi]$
 $\omega_i \in [\omega_0 - \Delta\omega/2, \omega_0 + \Delta\omega/2]$

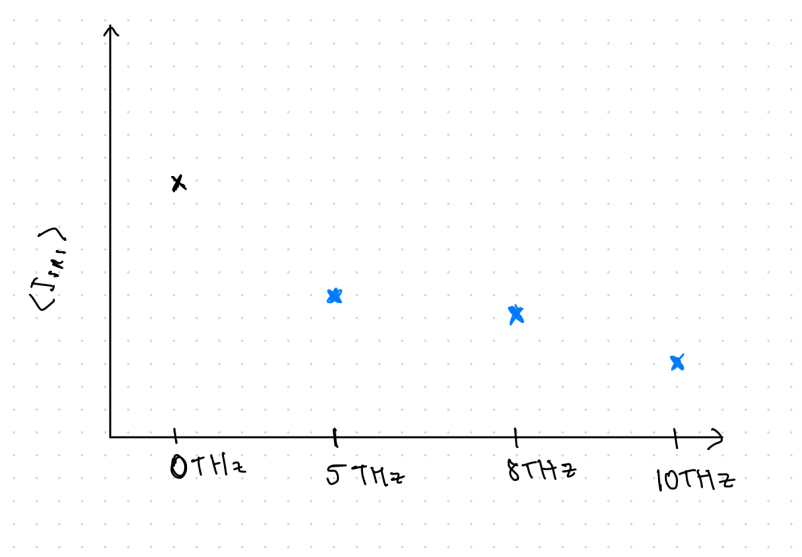


Figure 5.4: placeholder figure for ArF sim results

5.7 Conclusion

Chapter 6

Effects of an External Magnetic Field on Stimulated Raman Scattering

In this chapter, we present work performed while employed as a Junior Specialist at the University of California, San Diego between January and April 2020. The project was supervised by Professor Farhat Beg, and lead by Dr Adam Higginson (now at University of Boulder). The work presented (including data generated and data analysis) was carried out by the author, except in the cases outline below:

- Figure 6.2 SRS reflectivity from LULI, made by Matthieu

The chapter begins with a review of the literature which discusses the effect of an externally-applied magnetic field on stimulated Raman scattering. We then present modelling, performed by the author, of an experiment performed at the Laboratoire pour l'Utilisation des Lasers Intenses (France): J. R. Marquès, P. Loiseau, J. Béard, A. Castan, B. Coleman, T. Gangolf, L. Lancia, A. Soloviev, O. Portugall, and J. Fuchs. Analysis of the SRS diagnostics was performed by J. R. Marqès, and (revisited) by M. Bailly-Grandvaux. The experiment showed a small increase in SRS with an applied magnetic field, and this is recreated in our simulations. We then go on to investigate how the effect of the magnetic field depends on $k_{EPW}\lambda_D$ of the SRS electron plasma wave.

N.B. In this section, all simulations are driven by a 1ω Nd:glass laser with λ_0 . This is different to Chapter 4, which used the third harmonic of Nd:glass ($\lambda_0 = 351\text{nm}$) and Chapter 5 which

6.1 Motivation and literature review

Once again, wjhy is this a problem? why can we model in 1D?

How can we continue to only consider modes without B field? Why no X or O modes?

6.1.1 Magnetic field suppresses kinetic SRS

here's a recent paper about 90T fields effect on SRS in inhomogeneous plasmas [Zhou et al., 2021].

Start by replicating results from Winjum et al. [2018]

We started by replicating the results from Winjum et al. [2018].

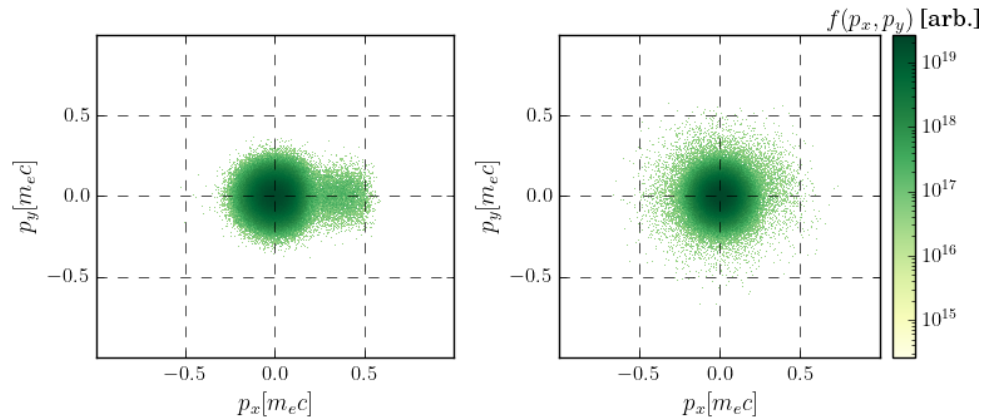


Figure 6.1: cf 0T (left) and 30T (right)

Suppress SRS to reduce harmful electrons and reflectivity, or enhance if it actually makes good electrons (in the case of shock-ignition)

6.1.2 Magnetic field could enhance kinetic SRS

6.1.3 What about fluid SRS?

6.2 Modelling SRS on LULI

6.2.1 Experimental results

6.2.2 Simulation results

Plasma density and temperature profiles at the centre of the gas jet were simulated using the FLASH code by Adam Higginson.

6.3 Magnetic field effect varies with plasma debye length

[Feng et al., 2018] REALLY good reference about SRS and LDI and anti-LDI

also don't forget this great paper about kld sclng of iSRS autoresonance [Chapman et al., 2013]

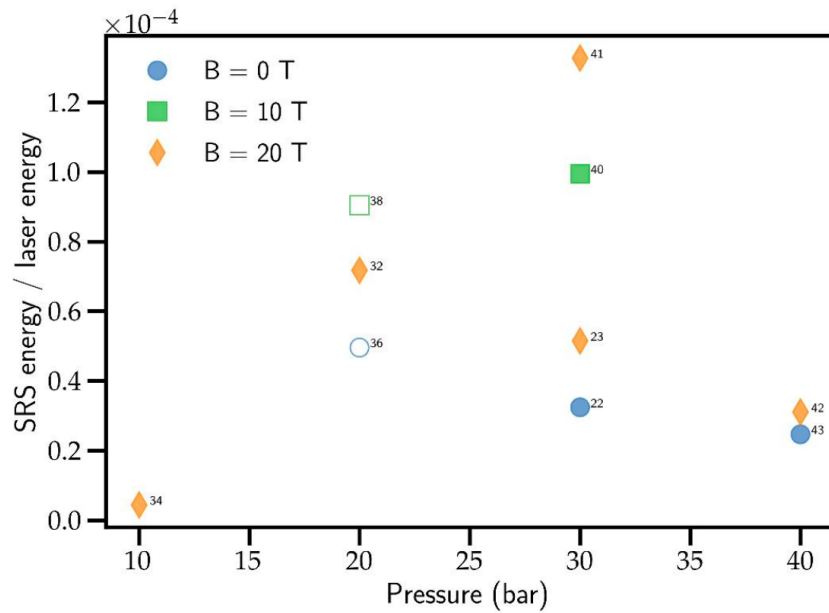


Figure 6.2: **Figure produced by M. Bailly-Grandvaux.** Experimentally-measured SRS energy at different gas jet pressures, with and without magnetic fields. The solid-coloured markers represent shots with the laser horizontally polarised with respect to the applied magnetic field, so that the laser magnetic field and applied magnetic field are parallel. The un-filled markers represent vertical polarisation of the laser.

n_e / n_{cr}	T_e / eV	bSRS $k_{\text{EPW}}\lambda_D$	fSRS $k_{\text{EPW}}\lambda_D$
0.01	180	0.36	0.02
0.025	450	0.34	0.03
0.05	600	0.27	0.04
0.10	900	0.21	0.05
0.15	1100	0.18	0.06

Table 6.1: T_i is $T_e/3$ in all cases

6.3.1 Fixed ions: vary $k_{\text{EPW}}\lambda_D$

Plasma parameters chosen to be relevant to LULI experiment (ish). $\lambda_0 = 1053\text{nm}$; $L_x = 1000\mu\text{m}$; $T_e = 1\text{keV}$; $I_0 = 1 \times 10^{15}\text{W/cm}^2$; $T_{\text{end}} = 10\text{ps}$; 1000 PPC (from convergence testing on $\langle I_{\text{SRS}} \rangle_{t>0}$).

6.4 Magnetic field effect changes with polarisation

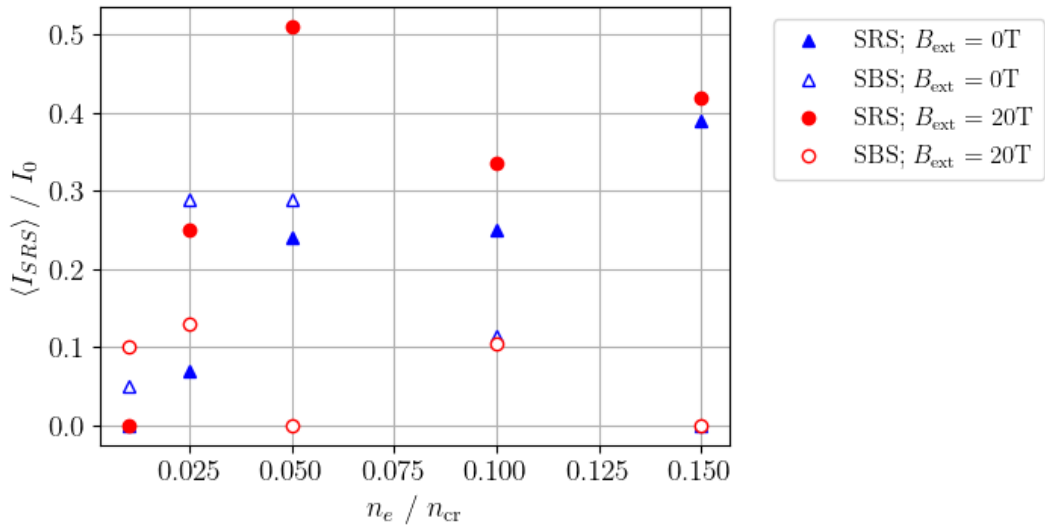
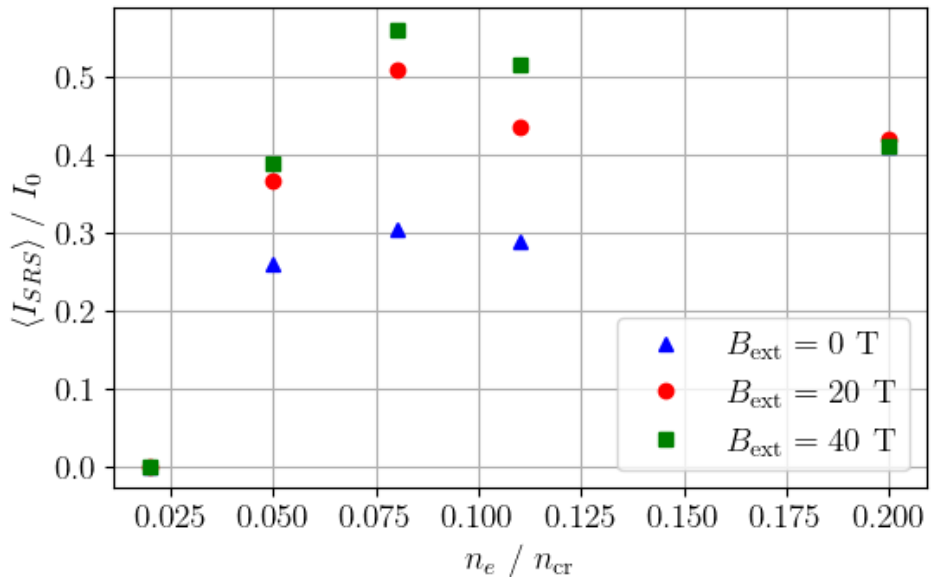


Figure 6.3: MAthieu made this

n_e / n_{cr}	$k_{EPW}\lambda_D$	regime	predicted behaviour
0.02	0.55	beyond “loss of resonance”	no SRS, no dependence on B_{ext}
0.05	0.33	strongly kinetic	
0.08	0.25	kinetic	
0.11	0.20	weakly kinetic	
0.20	0.12	fluid	no dependence on B_{ext}

Table 6.2: Plasma density, $k_{EPW}\lambda_D$, regime, predicted behaviourFigure 6.4: I made this. Parameters constant to all sims: $\lambda_0 = 1056\text{nm}$; $L_x = 1000\mu\text{m}$; $T_e = 1\text{keV}$; $I_0 = 1 \times 10^{15}\text{W/cm}^2$; $T_{end} = 10\text{ps}$; 1000 PPC.

Chapter 7

Conclusions and Future Work

7.1 Conclusion

7.1.1 Does any of this matter?

A recent paper by [Nicholas et al. \[2021\]](#) suggests that fusion energy (whether through ICF or magnetically confined fusion) will not be ready in time to act as a replacement for fossil fuels, which must be removed from the energy mix by the middle of the 21st century if we are to avoid the worst impacts of catastrophic climate change. They assume that, by the second half of the 21st century, renewable energies such as wind and solar will power most of the grid. However, the intermittent nature of these mechanisms will leave a gap in the energy market for a carbon-free source of baseload energy [[Nicholas et al., 2021](#)]. In order for fusion energy to be a good choice for filling this gap it must be able to demonstrate its superiority over traditional nuclear fission power generation. This may include showing its better performance in terms of: waste production; ease of proliferation; and resource supply. In light of this analysis, the work presented in this thesis may never directly contribute to usable, or desirable, ICF energy-generation schemes.

7.2 Future Work

7.3 Summary

Appendix A

License Agreements

AIP PUBLISHING LICENSE
TERMS AND CONDITIONS

Jan 06, 2021

This Agreement between SJ Spencer ("You") and AIP Publishing ("AIP Publishing") consists of your license details and the terms and conditions provided by AIP Publishing and Copyright Clearance Center.

License Number 4982981039259

License date Jan 06, 2021

Licensed Content Publisher AIP Publishing

Licensed Content Publication Physics of Plasmas

Licensed Content Title Inflationary stimulated Raman scattering in shock-ignition plasmas

Licensed Content Author S. J. Spencer, A. G. Seaton, T. Goffrey, et al

Licensed Content Date Dec 1, 2020

Licensed Content Volume 27

Licensed Content Issue 12

Type of Use Thesis/Dissertation

Requestor type Author (original article)

Format Print and electronic

Portion Excerpt (> 800 words)

Will you be translating? No

Title Particle-in-cell simulations of stimulated Raman scattering in the kinetic regime for direct-drive inertial confinement fusion

Institution name University of Warwick

Expected presentation date Sep 2021

Portions All figures and their captions; paragraphs 5-9; Table 1; all of section 2; derivation presented in section 3; all of Section 4

SJ Spencer
480 Banbury RoadRequestor Location
Oxford, OX2 8EN
United Kingdom
Attn: SJ Spencer

Total

0.00 GBP

Terms and Conditions

AIP Publishing -- Terms and Conditions: Permissions Uses

AIP Publishing hereby grants to you the non-exclusive right and license to use and/or distribute the Material according to the use specified in your order, on a one-time basis, for the specified term, with a maximum distribution equal to the number that you have ordered. Any links or other content accompanying the Material are not the subject of this license.

1. You agree to include the following copyright and permission notice with the reproduction of the Material: "Reprinted from [FULL CITATION], with the permission of AIP Publishing." For an article, the credit line and permission notice must be printed on the first page of the article or book chapter. For photographs, covers, or tables, the notice may appear with the Material, in a footnote, or in the reference list.
2. If you have licensed reuse of a figure, photograph, cover, or table, it is your responsibility to ensure that the material is original to AIP Publishing and does not contain the copyright of another entity, and that the copyright notice of the figure, photograph, cover, or table does not indicate that it was reprinted by AIP Publishing, with permission, from another source. Under no circumstances does AIP Publishing purport or intend to grant permission to reuse material to which it does not hold appropriate rights.
You may not alter or modify the Material in any manner. You may translate the Material into another language only if you have licensed translation rights. You may not use the Material for promotional purposes.
3. The foregoing license shall not take effect unless and until AIP Publishing or its agent, Copyright Clearance Center, receives the Payment in accordance with Copyright Clearance Center Billing and Payment Terms and Conditions, which are incorporated herein by reference.
4. AIP Publishing or Copyright Clearance Center may, within two business days of granting this license, revoke the license for any reason whatsoever, with a full refund payable to you. Should you violate the terms of this license at any time, AIP Publishing, or Copyright Clearance Center may revoke the license with no refund to you. Notice of such revocation will be made using the contact information provided by you. Failure to receive such notice will not nullify the revocation.
5. AIP Publishing makes no representations or warranties with respect to the Material. You agree to indemnify and hold harmless AIP Publishing, and their officers, directors, employees or agents from and against any and all claims arising out of your use of the Material other than as specifically authorized herein.
6. The permission granted herein is personal to you and is not transferable or assignable without the prior written permission of AIP Publishing. This license may not be amended except in a writing signed by the party to be charged.
7. If purchase orders, acknowledgments or check endorsements are issued on any forms containing terms and conditions which are inconsistent with these provisions, such inconsistent terms and conditions shall be of no force and effect. This document, including the CCC Billing and Payment Terms and Conditions, shall be the entire agreement between the parties relating to the subject matter hereof.

This Agreement shall be governed by and construed in accordance with the laws of the State of New York. Both parties hereby submit to the jurisdiction of the courts of New York County for purposes of resolving any disputes that may arise hereunder.

V1.2

**Questions? customercare@copyright.com or +1-855-239-3415
(toll free in the US) or +1-978-646-2777.**



American Physical Society Reuse and Permissions License

04-Feb-2021

This license agreement between the American Physical Society ("APS") and SJ Spencer ("You") consists of your license details and the terms and conditions provided by the American Physical Society and SciPris.

Licensed Content Information

License Number:	RNP/21/FEB/036065
License date:	04-Feb-2021
DOI:	10.1103/PhysRevLett.103.045004
Title:	Shock Ignition: A New Approach to High Gain Inertial Confinement Fusion on the National Ignition Facility
Author:	L. J. Perkins et al.
Publication:	Physical Review Letters
Publisher:	American Physical Society
Cost:	USD \$ 0.00

Request Details

Does your reuse require significant modifications:	No
Specify intended distribution locations:	Worldwide
Reuse Category:	Reuse in a thesis/dissertation
Requestor Type:	Student
Items for Reuse:	Figures/Tables
Number of Figure/Tables:	1
Figure/Tables Details:	Figure 1 parts a and b, caption text to be adapted.
Format for Reuse:	Print and Electronic
Total number of print copies:	Up to 1000

Information about New Publication:

University/Publisher:	University of Warwick, Coventry
Title of dissertation/thesis:	Particle-in-cell simulations of stimulated Raman scattering in the kinetic regime for direct-drive inertial confinement fusion
Author(s):	SJ Spencer
Expected completion date:	Sep. 2021

License Requestor Information

Name:	SJ Spencer
Affiliation:	Individual
Email Id:	sj_spencer@outlook.com
Country:	United Kingdom



TERMS AND CONDITIONS

The American Physical Society (APS) is pleased to grant the Requestor of this license a non-exclusive, non-transferable permission, limited to Print and Electronic format, provided all criteria outlined below are followed.

1. You must also obtain permission from at least one of the lead authors for each separate work, if you haven't done so already. The author's name and affiliation can be found on the first page of the published Article.
2. For electronic format permissions, Requestor agrees to provide a hyperlink from the reprinted APS material using the source material's DOI on the web page where the work appears. The hyperlink should use the standard DOI resolution URL, <http://dx.doi.org/{DOI}>. The hyperlink may be embedded in the copyright credit line.
3. For print format permissions, Requestor agrees to print the required copyright credit line on the first page where the material appears: "Reprinted (abstract/excerpt/figure) with permission from [(FULL REFERENCE CITATION) as follows: Author's Names, APS Journal Title, Volume Number, Page Number and Year of Publication.] Copyright (YEAR) by the American Physical Society."
4. Permission granted in this license is for a one-time use and does not include permission for any future editions, updates, databases, formats or other matters. Permission must be sought for any additional use.
5. Use of the material does not and must not imply any endorsement by APS.
6. APS does not imply, purport or intend to grant permission to reuse materials to which it does not hold copyright. It is the requestor's sole responsibility to ensure the licensed material is original to APS and does not contain the copyright of another entity, and that the copyright notice of the figure, photograph, cover or table does not indicate it was reprinted by APS with permission from another source.
7. The permission granted herein is personal to the Requestor for the use specified and is not transferable or assignable without express written permission of APS. This license may not be amended except in writing by APS.
8. You may not alter, edit or modify the material in any manner.
9. You may translate the materials only when translation rights have been granted.
10. APS is not responsible for any errors or omissions due to translation.
11. You may not use the material for promotional, sales, advertising or marketing purposes.
12. The foregoing license shall not take effect unless and until APS or its agent, Aptara, receives payment in full in accordance with Aptara Billing and Payment Terms and Conditions, which are incorporated herein by reference.
13. Should the terms of this license be violated at any time, APS or Aptara may revoke the license with no refund to you and seek relief to the fullest extent of the laws of the USA. Official written notice will be made using the contact information provided with the permission request. Failure to receive such notice will not nullify revocation of the permission.
14. APS reserves all rights not specifically granted herein.
15. This document, including the Aptara Billing and Payment Terms and Conditions, shall be the entire agreement between the parties relating to the subject matter hereof.

Bibliography

- T. D. Arber, K. Bennet, C. S. Brady, A. Lawrence-Douglas, M. G. Ramsay, N. J. Sircombe, P. Gillies, R. G. Evans, H. Schmitz, A. R. Bell, and C. P. Ridgers. Contemporary particle-in-cell approach to laser-plasma modeling. *Plasma Physics and Controlled Fusion*, 57:113001, 2015. doi: 10.1088/0741-3335/57/11/113001. URL <https://doi.org/10.1088/0741-3335/57/11/113001>.
- J.W. Bates, R.K. Follett, J.G. Shaw, S.P. Obenschain, R.H. Lehmberg, J.F. Myatt, J.L. Weaver, D.M. Kehne, M.F. Wolford, M.C. Myers, and T.J. Kessler. Suppressing cross-beam energy transfer with broadband lasers. *High Energy Density Physics*, 36:100772, 2020. ISSN 1574-1818. doi: <https://doi.org/10.1016/j.hedp.2020.100772>. URL <https://www.sciencedirect.com/science/article/pii/S1574181820300501>.
- S. D. Baton, A. Colaïtis, C. Rousseaux, G. Boutoux, S. Brygoo, L. Jacquet, M. Koenig, D. Batani, A. Casner, E. Le Bel, D. Raffestin, A. Tentori, V. Tikhonchuk, J. Trella, C. Reverdin, L. Le-Deroff, W. Theobald, G. Cristoforetti, L. A. Gizzi, P. Koester, L. Labate, and K. Shigemori. Preliminary results from the LMJ-PETAL experiment on hot electrons characterization in the context of shock ignition. *High Energy Density Physics*, 36(March):100796, 2020. ISSN 15741818. doi: 10.1016/j.hedp.2020.100796. URL <https://doi.org/10.1016/j.hedp.2020.100796>.
- C.K. Birdsall and A.B. Langdon. *Plasma Physics via Computer Simulation*. Series in Plasma Physics and Fluid Dynamics. Taylor & Francis, 1st edition, 1991. ISBN 0-07-005371-5. URL <https://doi.org/10.1201/9781315275048>.
- N. Carpintero-Santamaría and G. Velarde. The pioneers' legacy of inertial confinement nuclear fusion. *Progress in Nuclear Energy*, 78:349 – 354, 2015. ISSN 0149-1970. doi: 10.1016/j.pnucene.2013.10.019. URL <https://doi.org/10.1016/j.pnucene.2013.10.019>.
- T. Chapman, S. Hüller, P. E. Masson-Laborde, W. Rozmus, and D. Pesme. Spatially autoresonant stimulated Raman scattering in inhomogeneous plasmas in the kinetic regime. *Physics of Plasmas*, 17(12), 2010. ISSN 1070664X. doi: 10.1063/1.3529362. URL <https://doi.org/10.1063/1.3529362>.
- T. Chapman, S. Hüller, P. E. Masson-Laborde, A. Heron, D. Pesme, and W. Rozmus. Driven spatially autoresonant stimulated raman scattering in the kinetic regime. *Phys. Rev. Lett.*, 108:145003, Apr 2012. URL <https://doi.org/10.1103/PhysRevLett.108.145003>.
- T. Chapman, S. Hüller, P.E. Masson-Laborde, A. Heron, W. Rozmus, and D. Pesme. The dependence of spatial autoresonance in srs on k_l . *EPJ Web of Conferences*, 59:05012, 2013. doi: 10.1051/epjconf/20135905012. URL <https://doi.org/10.1051/epjconf/20135905012>.

- G. Cristoforetti, A. Colaitis, L. Antonelli, S. Atzeni, F. Baffigi, D. Batani, F. Barbato, G. Boutoux, R. Dudzak, P. Koester, E. Krousky, L. Labate, Ph Nicolaï, O. Renner, M. Skoric, V. Tikhonchuk, and L. A. Gizzi. Experimental observation of parametric instabilities at laser intensities relevant for shock ignition. *EPL*, 117(3), 2017. ISSN 12864854. URL <https://doi.org/10.1209/0295-5075/117/35001>.
- M. E. Dieckmann, S. J. Spencer, M. Falk, and G. Rowlands. Preferential acceleration of positrons by a filamentation instability between an electron–proton beam and a pair plasma beam. *Physics of Plasmas*, 27(12):122102, 2020. doi: 10.1063/5.0021257. URL <https://doi.org/10.1063/5.0021257>.
- I. N. Ellis, D. J. Strozzi, B. J. Winjum, F. S. Tsung, T. Grismayer, W. B. Mori, J. E. Fahlen, and E. A. Williams. Convective raman amplification of light pulses causing kinetic inflation in inertial fusion plasmas. *Physics of Plasmas*, 19(11):112704, November 2012. URL <https://doi.org/10.1063/1.4762853>.
- Roger Evans. UK fusion breakthrough revealed at last. *Physics World*, 23(03):23–23, mar 2010. doi: 10.1088/2058-7058/23/03/34. URL <https://doi.org/10.1088/2058-7058/23/03/34>.
- Q. S. Feng, C. Y. Zheng, Z. J. Liu, L. H. Cao, Q. Wang, C. Z. Xiao, and X. T. He. Anti-langmuir decay instability in langmuir decay instability cascade. *Physics of Plasmas*, 25(9):092112, 2018. doi: 10.1063/1.5041480. URL <https://doi.org/10.1063/1.5041480>.
- Juan C. Fernández, J. A. Cobble, D. S. Montgomery, M. D. Wilke, and B. B. Afeyan. Observed insensitivity of stimulated Raman scattering on electron density. *Physics of Plasmas*, 7(9):3743–3750, 2000. ISSN 1070664X. doi: 10.1063/1.1287134. URL <https://doi.org/10.1063/1.1287134>.
- R. K. Follett, J. G. Shaw, J. F. Myatt, C. Dorrer, D. H. Froula, and J. P. Palastro. Thresholds of absolute instabilities driven by a broadband laser. *Physics of Plasmas*, 26(6):062111, 2019. doi: 10.1063/1.5098479. URL <https://doi.org/10.1063/1.5098479>.
- R. K. Follett, J. G. Shaw, J. F. Myatt, H. Wen, D. H. Froula, and J. P. Palastro. Thresholds of absolute two-plasmon-decay and stimulated raman scattering instabilities driven by multiple broadband lasers. *Physics of Plasmas*, 28(3):032103, 2021. doi: 10.1063/5.0037869. URL <https://doi.org/10.1063/5.0037869>.
- P. N. Guzdar, C. S. Liu, and R. H. Lehmberg. The effect of bandwidth on the convective Raman instability in inhomogeneous plasmas. *Physics of Fluids B: Plasma Physics*, 3(10):2882–2888, October 1991. ISSN 0899-8221. doi: 10.1063/1.859921. URL <http://aip.scitation.org/doi/10.1063/1.859921>.
- A. Higginson, S. Zhang, M. Bailly-Grandvaux, C. McGuffey, K. Bhutwala, B. J. Winjum, J. Strehlow, B. Edghill, M. Dozieres, F. S. Tsung, R. Lee, S. Andrews, S. J. Spencer, N. Lemos, F. Albert, P. King, M. S. Wei, W. B. Mori, M. J.-E Manuel, and F. N. Beg. Electron acceleration at oblique angles via stimulated raman scattering at laser irradiance $> 10^{16} \text{Wcm}^{-2} \mu\text{m}^2$. *Phys. Rev. E*, 103:033203, Mar 2021. doi: 10.1103/PhysRevE.103.033203. URL <https://link.aps.org/doi/10.1103/PhysRevE.103.033203>.

- J. H. Kelly, A. Shvydky, J. A. Marozas, M. J. Guardalben, B. E. Kruschwitz, L. J. Waxer, C. Dorrer, E. Hill, A. V. Okishev, and J.-M. Di Nicola. Simulations of the propagation of multiple-fm smoothing by spectral dispersion on omega ep. *Proceedings of SPIE - The International Society for Optical Engineering*, 8602, 2 2013. doi: 10.1117/12.2003209. URL <https://doi.org/10.1117/12.2003209>.
- O. Klimo, J. Psikal, V. T. Tikhonchuk, and S. Weber. Two-dimensional simulations of laser-plasma interaction and hot electron generation in the context of shock-ignition research. *Plasma Physics and Controlled Fusion*, 56(5), 2014. ISSN 13616587. doi: 10.1088/0741-3335/56/5/055010. URL <https://doi.org/10.1088/0741-3335/56/5/055010>.
- J. L. Kline, D. S. Montgomery, L. Yin, D. F. DuBois, B. J. Albright, B. Bezzerides, J. A. Cobble, E. S. Dodd, D. F. DuBois, J. C. Fernández, R. P. Johnson, J. M. Kindel, H. A. Rose, H. X. Vu, and W. Daughton. Different $k\lambda D$ regimes for nonlinear effects on Langmuir waves. *Physics of Plasmas*, 13(5), 2006. ISSN 1070664X. URL <https://doi.org/10.1063/1.2178777>.
- W.L. Kruer. *The Physics of Laser Plasma Interactions*. CRC Press, 1st edition edition, 2003. ISBN 9781003003243. URL <https://doi.org/10.1201/9781003003243>.
- W.L. Kruer, K.G. Estabook, and K.H. Sinz. Instability-generated laser reflection in plasmas. *Nuclear Fusion*, 13(6):952–955, December 1973. doi: 10.1088/0029-5515/13/6/024. URL <https://doi.org/10.1088/0029-5515/13/6/024>.
- R. H. Lehmberg, M. F. Wolford, J. L. Weaver, D. Kehne, S. P. Obenschain, D. Eimerl, and J. P. Palastro. Stimulated rotational raman scattering of arbitrarily polarized broadband light. *Phys. Rev. A*, 102:063530, Dec 2020. doi: 10.1103/PhysRevA.102.063530. URL <https://link.aps.org/doi/10.1103/PhysRevA.102.063530>.
- R.H. Lehmberg and S.P. Obenschain. Use of induced spatial incoherence for uniform illumination of laser fusion targets. *Optics Communications*, 46(1):27–31, 1983. ISSN 0030-4018. doi: [https://doi.org/10.1016/0030-4018\(83\)90024-X](https://doi.org/10.1016/0030-4018(83)90024-X). URL <https://www.sciencedirect.com/science/article/pii/003040188390024X>.
- C S Liu and V K Tripathi. *Interaction of Electromagnetic Waves with Electron Beams and Plasmas*. World Scientific, 1994. doi: 10.1142/2189. URL <https://www.worldscientific.com/doi/abs/10.1142/2189>.
- T. H. Maiman. Stimulated optical radiation in ruby. *Nature*, 187(4736):493–494, August 1960. doi: 10.1038/187493a0. URL <https://doi.org/10.1038/187493a0>.
- D. S. Montgomery, J. A. Cobble, J. C. Fernández, R. J. Focia, R. P. Johnson, N. Renard-Legalloudec, H. A. Rose, and D. A. Russell. Recent Trident single hot spot experiments: Evidence for kinetic effects, and observation of Langmuir decay instability cascade. *Physics of Plasmas*, 9(5):2311–2320, 2002. doi: 10.1063/1.1468857. URL <https://doi.org/10.1063/1.1468857>.
- G. J. Morales and T. M. O’Neil. Nonlinear frequency shift of an electron plasma wave. *Phys. Rev. Lett.*, 28:417–420, Feb 1972. doi: 10.1103/PhysRevLett.28.417. URL <https://link.aps.org/doi/10.1103/PhysRevLett.28.417>.

- T.E.G. Nicholas, T.P. Davis, F. Federici, J. Leland, B.S. Patel, C. Vincent, and S.H. Ward. Re-examining the role of nuclear fusion in a renewables-based energy mix. *Energy Policy*, 149:112043, February 2021. doi: 10.1016/j.enpol.2020.112043. URL <https://doi.org/10.1016/j.enpol.2020.112043>.
- K. Nishikawa and C. S. Liu. *General formalism of parametric excitation*, volume 6, pages 3–81. 1976.
- J. Nuckolls, L. Wood, A. Thiessen, and G. Zimmerman. Laser compression of matter to super-high densities: Thermonuclear (CTR) applications. *Nature*, 239(5368):139–142, September 1972. doi: 10.1038/239139a0. URL <https://doi.org/10.1038/239139a0>.
- S. P. Obenschain, A. J. Schmitt, J. W. Bates, M. F. Wolford, M. C. Myers, M. W. McGeoch, M. Karasik, and J. L. Weaver. Direct drive with the argon fluoride laser as a path to high fusion gain with sub-megajoule laser energy. *Philosophical Transactions of the Royal Society A: Mathematical, Physical and Engineering Sciences*, 378(2184):20200031, 2020. doi: 10.1098/rsta.2020.0031. URL <https://royalsocietypublishing.org/doi/abs/10.1098/rsta.2020.0031>.
- Stephen Obenschain, Robert Lehmberg, David Kehne, Frank Hegeler, Matthew Wolford, John Sethian, James Weaver, and Max Karasik. High-energy krypton fluoride lasers for inertial fusion. *Appl. Opt.*, 54(31):F103–F122, Nov 2015. doi: 10.1364/AO.54.00F103. URL <http://ao.osa.org/abstract.cfm?URI=ao-54-31-F103>.
- T. O’Neil. *Physics of Fluids*, 12(8), 1965. URL <https://doi.org/10.1063/1.1761193>.
- L. J. Perkins, R. Betti, K. N. LaFortune, and W. H. Williams. Shock ignition: A new approach to high gain inertial confinement fusion on the national ignition facility. *Phys. Rev. Lett.*, 103: 045004, Jul 2009. doi: 10.1103/PhysRevLett.103.045004. URL <https://link.aps.org/doi/10.1103/PhysRevLett.103.045004>.
- M. G. Raymer, J. Mostowski, and J. L. Carlsten. Theory of stimulated Raman scattering with broad-band lasers. *Physical Review A*, 19(6):2304–2316, June 1979. ISSN 0556-2791. doi: 10.1103/PhysRevA.19.2304. URL <https://link.aps.org/doi/10.1103/PhysRevA.19.2304>.
- Sean P. Regan, John A. Marozas, R. Stephen Craxton, John H. Kelly, William R. Donaldson, Paul A. Jaanimagi, Douglas Jacobs-Perkins, Robert L. Keck, Terrance J. Kessler, David D. Meyerhofer, T. Craig Sangster, Wolf Seka, Vladimir A. Smalyuk, Stanley Skupsky, and Jonathan D. Zuegel. Performance of 1-thz-bandwidth, two-dimensional smoothing by spectral dispersion and polarization smoothing of high-power, solid-state laser beams. *J. Opt. Soc. Am. B*, 22(5):998–1002, May 2005. doi: 10.1364/JOSAB.22.000998. URL <http://josab.osa.org/abstract.cfm?URI=josab-22-5-998>.
- X Ribeyre, G Schurtz, M Lafon, S Galera, and S Weber. Shock ignition: an alternative scheme for HiPER. *Plasma Physics and Controlled Fusion*, 51(1):015013, dec 2009. URL <https://iopscience.iop.org/article/10.1088/0741-3335/51/1/015013/meta>.
- C. Riconda, S. Weber, V. T. Tikhonchuk, and A. Héron. Kinetic simulations of stimulated Raman backscattering and related processes for the shock-ignition approach to inertial confinement fusion. *Physics of Plasmas*, 18(9), 2011. ISSN 1070664X. doi: 10.1063/1.3630937. URL <https://doi.org/10.1063/1.3630937>.

- H. A. Rose and D. A. Russell. A self-consistent trapping model of driven electron plasma waves and limits on stimulated Raman scatter. *Physics of Plasmas*, 8(11):4784–4799, 2001. ISSN 1070664X. doi: 10.1063/1.1410111. URL <https://doi.org/10.1063/1.1410111>.
- M. J. Rosenberg, A. A. Solodov, W. Seka, R. K. Follett, J. F. Myatt, A. V. Maximov, C. Ren, S. Cao, P. Michel, M. Hohenberger, J. P. Palastro, C. Goyon, T. Chapman, J. E. Ralph, J. D. Moody, R. H. H. Scott, K. Glize, and S. P. Regan. Stimulated raman scattering mechanisms and scaling behavior in planar direct-drive experiments at the national ignition facility. *Physics of Plasmas*, 27(4):042705, 2020. doi: 10.1063/1.5139226. URL <https://doi.org/10.1063/1.5139226>.
- M. N. Rosenbluth. Parametric Instabilities in Inhomogeneous Media. *Physical Review Letters*, 29(9):565, 1972. doi: 10.1103/PhysRevLett.29.565.
- C. Rousseaux, L. Gremillet, M. Casanova, P. Loiseau, M. Rabec Le Gloahec, S. D. Baton, F. Amiranoff, J. C. Adam, and A. Héron. Transient development of backward stimulated Raman and Brillouin scattering on a picosecond time scale measured by subpicosecond thomson diagnostic. *Physical Review Letters*, 97(1):1–4, 2006. ISSN 10797114. URL <https://doi.org/10.1103/PhysRevLett.108.145003>.
- Roald Z. Sagdeev and Patrick H. Diamond. An interview with roald sagdeev: his story of plasma physics in russia, 1956–1988. *The European Physical Journal H*, 43(4–5):355–396, October 2018. doi: 10.1140/epjh/e2018-90042-3. URL <https://doi.org/10.1140/epjh/e2018-90042-3>.
- A. L. Schawlow and C. H. Townes. Infrared and optical masers. *Phys. Rev.*, 112:1940–1949, Dec 1958. doi: 10.1103/PhysRev.112.1940. URL <https://link.aps.org/doi/10.1103/PhysRev.112.1940>.
- S. Skupsky, R. W. Short, T. Kessler, R. S. Craxton, S. Letzring, and J. M. Soures. Improved laser-beam uniformity using the angular dispersion of frequency-modulated light. *Journal of Applied Physics*, 66(8):3456–3462, 1989. doi: 10.1063/1.344101. URL <https://doi.org/10.1063/1.344101>.
- S. J. Spencer, A. G. Seaton, T. Goffrey, and T. D. Arber. Inflationary stimulated Raman scattering in shock-ignition plasmas. *Physics of Plasmas*, 27(12):122705, 2020. doi: 10.1063/5.0022901. URL <https://doi.org/10.1063/5.0022901>.
- D. J. Strozzi, E. A. Williams, A. B. Langdon, and A. Bers. Kinetic enhancement of raman backscatter, and electron acoustic thomson scatter. *Physics of Plasmas*, 14(1):013104, January 2007. doi: 10.1063/1.2431161. URL <https://doi.org/10.1063/1.2431161>.
- J. J. Thomson and Jack I. Karush. Effects of finite-bandwidth driver on the parametric instability. *The Physics of Fluids*, 17(8):1608–1613, 1974. doi: 10.1063/1.1694940. URL <https://aip.scitation.org/doi/abs/10.1063/1.1694940>.
- G. Tran, P. Loiseau, A. Fusaro, A. Héron, S. Hüller, L. Maëder, P.-E. Masson-Laborde, D. Peninckx, and G. Riazuelo. Fluid modeling of stimulated raman scattering accounting for trapped particles benchmarked against fully kinetic simulations. *Physics of Plasmas*, 27(12):122707, 2020. doi: 10.1063/5.0018669. URL <https://doi.org/10.1063/5.0018669>.

- H. X. Vu, D F Dubois, and B Bezzerides. Transient Enhancement and Detuning of Laser-Driven Parametric Instabilities by Particle Trapping. *Physical Review Letters*, (June), 2001. doi: 10.1103/PhysRevLett.86.4306. URL <https://doi.org/10.1103/PhysRevLett.86.4306>.
- H. X. Vu, D. F. DuBois, and B. Bezzerides. Kinetic inflation of stimulated Raman backscatter in regimes of high linear Landau damping. *Physics of Plasmas*, 9(5):1745, 2002. ISSN 1070664X. doi: 10.1063/1.1471235. URL <https://doi.org/10.1063/1.1471235>.
- H. X. Vu, D. F. DuBois, and B. Bezzerides. Inflation threshold : A nonlinear trapping- induced threshold for the rapid onset of stimulated Raman scattering from a single laser speckle. *Physics of Plasmas*, 2007. doi: 10.1063/1.2426918. URL <https://doi.org/10.1063/1.2426918>.
- Y. X. Wang, Q. Wang, C. Y. Zheng, Z. J. Liu, C. S. Liu, and X. T. He. Nonlinear transition from convective to absolute Raman instability with trapped electrons and inflationary growth of reflectivity. *Physics of Plasmas*, 25(10), 2018. ISSN 10897674. doi: 10.1063/1.5040095. URL <https://doi.org/10.1063/1.5040095>.
- E. W. Weisstein. ‘fourier transform. from mathworld—a wolfram web resource. <http://mathworld.wolfram.com/FourierTransform.html>. Accessed: 02-06-2021.
- H. Wen, R. K. Follett, A. V. Maximov, D. H. Froula, F. S. Tsung, and J. P. Palastro. Suppressing the enhancement of stimulated raman scattering in inhomogeneous plasmas by tuning the modulation frequency of a broadband laser. *Physics of Plasmas*, 28(4):042109, 2021. doi: 10.1063/5.0036768. URL <https://doi.org/10.1063/5.0036768>.
- E. A. Williams. Convective growth of parametrically unstable modes in inhomogeneous media. *Physics of Fluids B: Plasma Physics*, 3(6):1504–1506, 1991. doi: 10.1063/1.859719. URL <https://doi.org/10.1063/1.859719>.
- B. J. Winjum, F. S. Tsung, and W. B. Mori. Mitigation of stimulated Raman scattering in the kinetic regime by external magnetic fields. *Physical Review E*, 98(4):1–5, 2018. ISSN 24700053. doi: 10.1103/PhysRevE.98.043208. URL <https://link.aps.org/doi/10.1103/PhysRevE.98.043208>.
- B. J. Winjum, A. Tableman, F. S. Tsung, and W. B. Mori. Interactions of laser speckles due to kinetic stimulated raman scattering. *Physics of Plasmas*, 26(11):112701, 2019. doi: 10.1063/1.5110513. URL <https://doi.org/10.1063/1.5110513>.
- L. Yin, W. Daughton, B. J. Albright, K. J. Bowers, D. S. Montgomery, J. L. Kline, J. C. Fernández, and Q. Roper. Nonlinear backward stimulated Raman scattering from electron beam acoustic modes in the kinetic regime. *Physics of Plasmas*, 13(7), 2006. ISSN 1070664X. URL <https://doi.org/10.1063/1.2210929>.
- L. Yin, B. J. Albright, K. J. Bowers, W. Daughton, and H. A. Rose. Saturation of backward stimulated scattering of a laser beam in the kinetic regime. *Phys. Rev. Lett.*, 99:265004, Dec 2007. doi: 10.1103/PhysRevLett.99.265004. URL <https://link.aps.org/doi/10.1103/PhysRevLett.99.265004>.
- L. Yin, B. J. Albright, K. J. Bowers, W. Daughton, and H. A. Rose. Saturation of backward stimulated scattering of laser in kinetic regime: Wavefront bowing, trapped particle modulational instability, and trapped particle self-focusing of plasma waves. *Physics of Plasmas*, 15 (1), 2008. ISSN 1070664X. URL <https://doi.org/10.1063/1.2825663>.

- L. Yin, B. J. Albright, H. A. Rose, K. J. Bowers, B. Bergen, R. K. Kirkwood, D. E. Hinkel, A. B. Langdon, P. Michel, D. S. Montgomery, and J. L. Kline. Trapping induced nonlinear behavior of backward stimulated Raman scattering in multi-speckled laser beams. *Physics of Plasmas*, 19(5), 2012. ISSN 1070664X. doi: 10.1063/1.3694673. URL <https://doi.org/10.1063/1.3694673>.
- Y. Zhao, L.-L. Yu, J. Zheng, S. Weng, C. Ren, C.-S. Liu, and Z.-M. Sheng. Effects of large laser bandwidth on stimulated raman scattering instability in underdense plasma. *Physics of Plasmas*, 22(5):052119, 2015. doi: 10.1063/1.4921659. URL <https://aip.scitation.org/doi/abs/10.1063/1.4921659>.
- Y. Zhao, S. Weng, M. Chen, J. Zheng, H. Zhuo, C. Ren, Z. Sheng, and J. Zhang. Effective suppression of parametric instabilities with decoupled broadband lasers in plasma. *Physics of Plasmas*, 24(11):112102, 2017a. doi: 10.1063/1.5003420. URL <https://doi.org/10.1063/1.5003420>.
- Y. Zhao, S. Weng, M. Chen, J. Zheng, H. Zhuo, and Z. Sheng. Stimulated raman scattering excited by incoherent light in plasma. *Matter and Radiation at Extremes*, 2(4):190–196, July 2017b. doi: 10.1016/j.mre.2017.06.001. URL <https://aip.scitation.org/doi/abs/10.1016/j.mre.2017.06.001>.
- Yao Zhao, Suming Weng, Zhengming Sheng, and Jianqiang Zhu. Suppression of parametric instabilities in inhomogeneous plasma with multi-frequency light. *Plasma Physics and Controlled Fusion*, 61(11):115008, oct 2019. doi: 10.1088/1361-6587/ab4691. URL <https://doi.org/10.1088/1361-6587/ab4691>.
- H. Y. Zhou, C. Z. Xiao, D. B. Zou, X. Z. Li, Y. Yin, F. Q. Shao, and H. B. Zhuo. Numerical study of bandwidth effect on stimulated raman backscattering in nonlinear regime. *Physics of Plasmas*, 25(6):062703, 2018. doi: 10.1063/1.5030153. URL <https://doi.org/10.1063/1.5030153>.
- Y. Z. Zhou, C. Y. Zheng, Z. K. Liu, and L. H. Cao. Suppression of autoresonant stimulated raman scattering in transversely weakly magnetized plasmas. *Plasma Physics and Controlled Fusion*, 63(5):055015, 2021. doi: 10.1088/1361-6587/abf253. URL <https://iopscience.iop.org/article/10.1088/1361-6587/abf253>.